

ALMA Central molecular zone Exploration Survey (ACES) IV: Data of the two intermediate-width spectral windows

Xing Lu,^{1,2} Daniel L. Walker,^{3*} Adam Ginsburg,⁴ Ashley T. Barnes,⁵ Pei-Ying Hsieh,⁶ Álvaro Sánchez-Monge,^{7,8} Savannah R. Gramze,⁴ Nazar Budaiev,⁴ Marc W. Pound,⁹ Jaime E. Pineda,¹⁰ Alyssa Bulatek,⁴ Claire Cook,¹¹ Jonathan D. Henshaw,^{12,13} Katharina Immer,⁵ Namitha Issac,¹ Desmond Jeff,⁴ Fu-Heng Liang,^{14,5} Steven N. Longmore,^{12,15} Elisabeth A.C. Mills,¹¹ Sergio Martín,^{16,17} Xing Pan,^{18,19,20} Qizhou Zhang,²⁰ John Bally,²¹ Cara Battersby,²² Laura Colzi,²³ Paul T. P. Ho,²⁴ Izaskun Jiménez-Serra,²³ J. M. Diederik Kruijssen,¹⁵ Maya A. Petkova,²⁵ Mattia C. Sormani,²⁶ Robin G. Tress,²⁷ Jennifer Wallace,²² J. Armijos-Abendaño,²⁸ Lucia Armillotta,²⁹ N. Bijas,³⁰ Rojita Buddhacharya,¹² Laura A. Busch,¹⁰ Natalie O. Butterfield,³¹ Mélanie Chevance,^{32,15} Ana Karla Díaz-Rodríguez,³ Christoph Federrath,³³ Rubén Fedriani,³⁴ Pablo García,^{35,36} Qi-Lao Gu,¹ H Perry Hatchfield,²² Rebecca J. Houghton,¹² Yue Hu,³⁷ Janik Karoly,³⁸ Ralf S. Klessen,^{32,39,20} Mark R. Krumholz,³³ Xunchuan Liu,¹ Farideh Mazoochi,⁴⁰ Francisco Nogueras-Lara,^{34,5} Dylan Paré,^{17,31} Denise Riquelme-Vásquez,⁴¹ Víctor M. Rivilla,²³ Miriam G. Santa-Maria,^{4,42} Anika Schmiedeke,⁴³ Yoshiaki Sofue,⁴⁴ Volker Tolls,²⁰ Q. Daniel Wang,⁴⁵ Gwenllian M. Williams,⁴⁶ Fengwei Xu,^{47,48} and Suinan Zhang^{49,6}

* Author affiliations are listed at the end of the paper

Accepted 2026 February 02. Received 2026 February 02; in original form 2025 July 18

ABSTRACT

We release the intermediate-width spectral window data from the ALMA Central Molecular Zone Exploration Survey (ACES) large program, which covers SiO (2–1), SO (2₂–1₁), H¹³CO⁺ (1–0), H¹³CN (1–0), HN¹³C (1–0), and HC¹⁵N (1–0), among other molecular line transitions, with an angular resolution of $\sim 2''$ and a velocity resolution of 1.7 km s^{-1} . The full cubes of the two spectral windows as well as the key data products will be available to the community. We also present the integrated brightness, peak brightness, centroid velocity, and Galactic longitude-velocity maps of the six lines. We briefly discuss morphological correlations between the continuum and the molecular line emission, and brightness ratios between pairs of isotopologue or isotopomer lines. We highlight features and trends in the data that will be followed up in upcoming ACES science papers.

Key words: Galactic: centre — ISM: structure

1 INTRODUCTION

The Central Molecular Zone (CMZ) usually refers to the central $\sim 500 \text{ pc}$ of our Galaxy, where $2\text{--}6 \times 10^7 M_{\odot}$ of molecular gas is detected (Ferrière et al. 2007; Henshaw et al. 2023). The distance to the supermassive black hole Sgr A* inside the CMZ is measured to 8.277 kpc (GRAVITY Collaboration et al. 2022), which is often adopted as the distance to the CMZ. The measured physical and chemical properties of the molecular gas are extreme compared to those of clouds in the Galactic disk, with e.g., higher temperatures

($\geq 50\text{--}100 \text{ K}$ vs $\sim 10\text{--}20 \text{ K}$; Ao et al. 2013; Mills & Morris 2013; Ginsburg et al. 2016b; Immer et al. 2016; Krieger et al. 2017; Lu et al. 2017), stronger non-thermal motions (FWHM $\sim 5\text{--}10 \text{ km s}^{-1}$ vs $\leq 1 \text{ km s}^{-1}$ at 0.1 pc to pc scales; Liu et al. 2013; Rathborne et al. 2014b; Henshaw et al. 2016a), and stronger magnetic fields ($\sim \text{mG}$ vs $\sim 0.01\text{--}0.1 \text{ mG}$; Pillai et al. 2015; Mangilli et al. 2019; Guan et al. 2021; Lu et al. 2024). The star formation rate (SFR) in the CMZ has been measured to be $\sim 0.07 M_{\odot} \text{ yr}^{-1}$ over the last 5 Myr, which is about 10% of the expected value given the well-established linear correlation between the amount of dense molecular gas and the SFR (Kauffmann et al. 2017; Barnes et al. 2017; Lu et al. 2019; Henshaw et al. 2023). Understanding how the physical conditions of the molecular gas are related to the inefficient star formation in the CMZ is an ongoing challenge that requires the combined insight from both observations and numerical simulations to elucidate the

* E-mail: daniel.walker.astro@gmail.com

† Elizabeth S. and Richard M. Cashin Fellow at the Radcliffe Institute for Advanced Studies at Harvard University, 10 Garden Street, Cambridge, MA 02138, USA

key physics (Kruijssen et al. 2014, 2019; Krumholz & Kruijssen 2015; Krumholz et al. 2017; Tress et al. 2020; Sormani et al. 2022).

A critical observational part of this challenge is to characterize the properties of the molecular gas with CMZ-wide surveys of molecular lines. There exist several surveys using single dish telescopes targeting the CO lines (e.g., Bally et al. 1987; Oka et al. 1998, 2007; Eden et al. 2020), the NH₃ inversion lines (e.g., Huettemeister et al. 1993; Arai et al. 2016; Longmore et al. 2017), and particularly, several 3 mm lines including SiO, H¹³CN, and H¹³CO⁺ that trace shocks or dense gas (e.g., Martín-Pintado et al. 1997; Riquelme et al. 2010a; Jones et al. 2012). Such observations have provided important constraints to modeling gas dynamics (e.g., Kruijssen et al. 2015; Henshaw et al. 2016b), heating and cooling of the gas (e.g., Ao et al. 2013; Ginsburg et al. 2016b; Immer et al. 2016), and chemistry (e.g., Martín-Pintado et al. 1997, 2000; Requena-Torres et al. 2006, 2008; Martín et al. 2008; Jones et al. 2012). However, interferometric observations with resolutions $\lesssim 2''$ are necessary to resolve molecular gas down to the spatial scales of individual dense cores (~ 0.1 pc) and uncover the immediate environment of star formation.

The ALMA CMZ Exploration Survey (ACES) Large Program uniformly covers the central ~ 200 pc of the CMZ using the Atacama Large Millimeter/submillimeter Array (ALMA) with its 3 mm band (Band 3), generating the largest mosaic ALMA has yet produced (>1000 arcmin²) with an unprecedented resolution of $\sim 2''$ (Project code: 2021.1.00172.L, PI: S. Longmore; Longmore & ACES Team 2026, hereafter Paper I). The main scientific objectives are to derive the physical, kinematic and chemical properties of the dense gas and protostellar and prestellar core population in the inner CMZ and use this to build a global understanding of star formation, feedback, and the mass flows and energy cycles across the Central Molecular Zone.

The observations captured the 3 mm continuum with an effective bandwidth of 4.6 GHz, which is released in Ginsburg & ACES Team (2026, hereafter Paper II). In addition to the continuum emission, three different setups of spectral windows (SPWs) were used to sample spectral lines: two narrow SPWs each with a total bandwidth of 58.59 MHz (~ 200 km s⁻¹) and an effective resolution of 0.06 MHz (~ 0.2 km s⁻¹), to cover HNCO (4–3) and HCO⁺ (1–0), respectively, which are released in Walker & ACES Team (2026, hereafter Paper III); two wide SPWs each with a total bandwidth of 1.875 GHz and an effective resolution of 0.976 MHz (~ 2.9 km s⁻¹), to cover various lines including CS (2–1), which are released in Hsieh & ACES Team (2026, hereafter Paper V); and two intermediate-width SPWs each with a total bandwidth of 0.469 GHz and a resolution of 0.488 MHz (~ 1.7 km s⁻¹, which characterises the ability to distinguish spectral features and is twice the physical channel width¹), which are released in this paper. The 12-m array, 7-m array, and the Total Power (TP, i.e., single-dish) array of ALMA were used for recovering structures of different spatial scales. The bandwidths of the spectral windows of the three arrays are different, with those of the 7-m and TP arrays slightly broader than that of the 12-m array to ensure effective data combination with the latter. In the following, we refer to the two intermediate-width SPWs as 12-m SPWs 25 and 27 (see Table 1), respectively.

¹ See <https://help.almascience.org/kb/articles/new-default-for-the-bandwidth-used-for-sensitivity-in-the-ot> for details.

2 OBSERVATIONS

General information about the observations can be found in the survey description paper (Paper I) and other data release papers (Paper II; Paper III; Paper V). Here we focus on the 12-m SPWs 25 and 27. The 12-m SPW 25 was centered at a rest frequency of 86.2 GHz and covered frequencies between 85.96 GHz and 86.43 GHz, which allows it to sample several spectral lines including HC¹⁵N (1–0), SO (2₂–1₁), and H¹³CN (1–0). The 12-m SPW 27 was centered at a rest frequency of 86.9 GHz, covering frequencies between 86.66 GHz and 87.13 GHz and spectral lines including H¹³CO⁺ (1–0), SiO (2–1), and HN¹³C (1–0). Figure 1 presents ACES spectra from a hot core in the top panel and those from a relatively quiescent core in the bottom. The difference in their chemistry is evident. Key properties of the six strong lines are listed in Table 1. In the following, we focus on those six lines and present their images and statistics, while other lines will be included in the data release but will not be discussed here.

3 DATA PROCESSING

3.1 Data reduction

The data were calibrated and imaged with the CASA package 6.5.4 (CASA Team et al. 2022). Procedures of continuum subtraction and array combination are described in Paper III. Note that in this data release, we have adopted the “feather-only” approach (see Paper III) to combine images from the three different arrays. In Appendix B, we describe an alternative method that employs the software package MIRIAD² (Sault et al. 1995) and a different approach to combine interferometer and single dish data. We have chosen not to apply this alternative method to the full ACES dataset, but invite interested readers to refer to Appendix B and references therein for further details.

The images of the two SPWs were produced with the *tclean* task in CASA. The native channel width is 0.244 MHz (~ 0.85 km s⁻¹), half of the spectral resolution, which was preserved in the imaging processes. For different regions in the large mosaic, slightly different imaging parameters (e.g., robustness number, pixel size) were chosen. Image cubes of different regions were then smoothed to a common beam and were stitched together to produce the final, full-CMZ mosaics. The cube of 12-m SPW 25 has a beam size of $3.17'' \times 2.15''$ with a position angle of -85.9° , while the cube of 12-m SPW 27 has a slightly larger beam of $3.25'' \times 2.26''$ with a position angle of -85.7° . The geometric mean of the beams is $\sim 2.6''$, corresponding to a linear resolution of 0.1 pc at a distance of 8.277 kpc. The image rms noise per 0.85 km s⁻¹ channel is not uniform across the mosaics, but varies between regions typically in the range of 3–5 mJy beam⁻¹, and can be much higher in the area surrounding regions of strong emission that limit the dynamic range.

3.2 Data products

The full cubes of the two SPWs are released at <https://almascience.org/alma-data/lp/aces>. For the six lines highlighted in Figure 1 and Table 1, we additionally provide their integrated brightness temperature maps, centroid velocity maps, peak brightness temperature maps, and Galactic longitude-velocity as well as Galactic latitude-velocity maps. Except otherwise noted, a customized mask

² <https://www.astro.umd.edu/~teuben/miriad/>

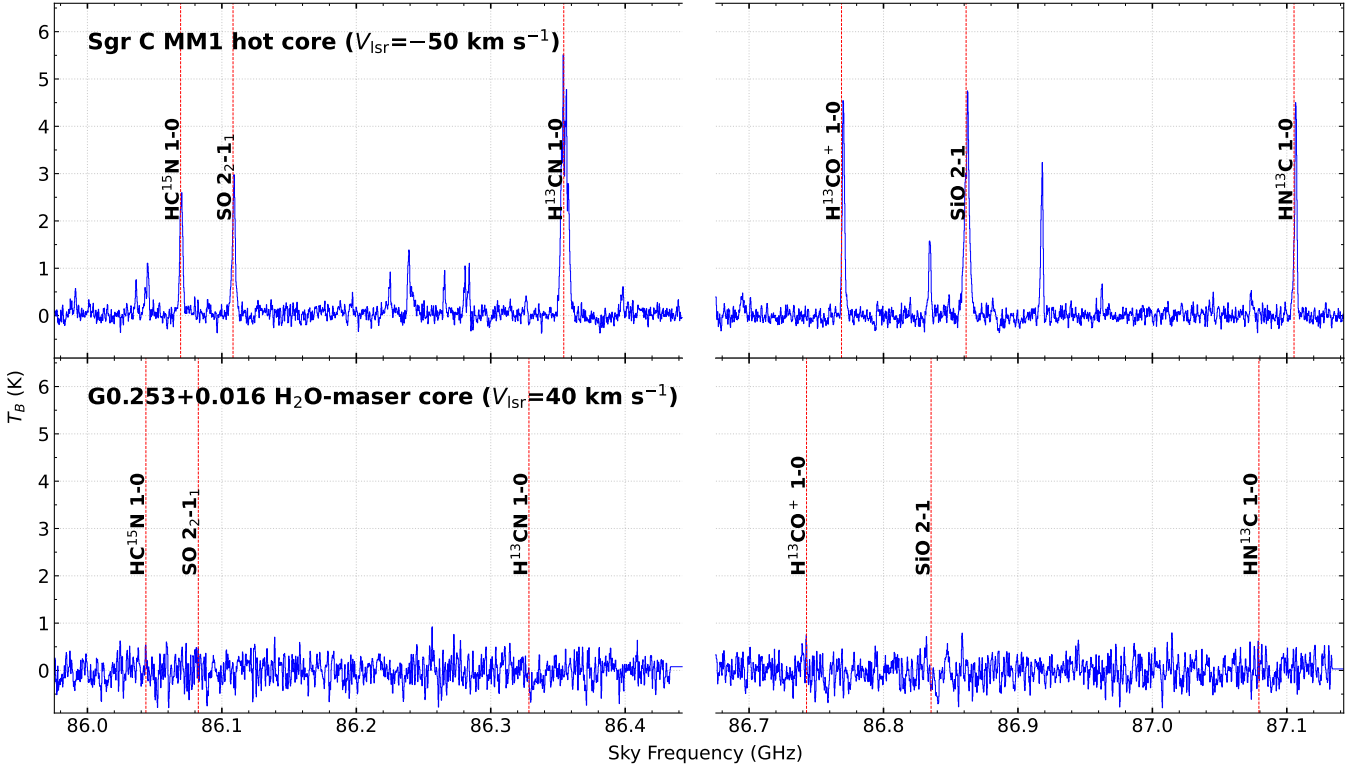


Figure 1. Typical spectra of the two SPWs toward a hot core (top) and a relatively quiescent core (bottom), respectively. The spectra are extracted and averaged from a circle with a radius of $0''.75$, centered at $(l, b) = (359.436^\circ, -0.104^\circ)$ and $(0.261^\circ, 0.016^\circ)$, respectively. The six transitions presented in this paper are labeled. There are other line emission features in the two SPWs that will not be discussed in this data release paper.

Table 1. Spectral configuration of the 12-m SPWs 25 and 27, and key spectral lines covered. The upper and lower frequency bounds of the SPWs are those of the 12-m array data.

SPW id (12-m/7-m/TP)	ν_L (MHz)	ν_U (MHz)	Molecule	Transition	Rest frequency (MHz)	E_u/k (K)	$\log(A_{ul})$ (s^{-1})	n_{crit}^a (cm^{-3})
25/16/17	85965.6	86434.4	HC ¹⁵ N	$J=1-0$	86054.97	4.13	-4.6569	2×10^6
			SO	$N_J=2_2-1_1$	86093.95	19.3	-5.2798	2×10^6
			H ¹³ CN	$J=1-0$	86339.92	4.14	-4.6526	2×10^6
27/18/19	86665.6	87134.4	H ¹³ CO ⁺	$J=1-0$	86754.30	4.16	-4.4141	2×10^5
			SiO	$J=2-1$	86846.96	6.25	-4.5336	2×10^5
			HN ¹³ C	$J=1-0$	87090.85	4.18	-4.5702	4×10^5

^a Critical densities are calculated as $n_{crit} = A_{ul}/\gamma_{ul}$, where A_{ul} is the Einstein coefficient and γ_{ul} is the collisional rate, whose values at 100 K are taken from the Leiden Atomic and Molecular Database (Schöier et al. 2005).

in the Galactic longitude-velocity plain (l - V_{LSR} mask hereafter) was applied when making the maps, which covers a velocity (V_{LSR}) range between -120 and 200 $km\ s^{-1}$ at Galactic longitude of 0.9° and between -220 and 100 $km\ s^{-1}$ at Galactic longitude of -0.6° , and linearly interpolates in between the two ends. These maps of the six lines are presented in Figures 2–11.

There are several considerations for the data products that warrant emphasis:

- The rest frequency of a SiO rotational-vibrational transition ($J=2-1$, $v=1$), often showing maser emission, is 86243.37 MHz, which is close to the frequency of H¹³CN. This SiO maser is usually excited in the envelopes of AGB stars, and has been found to be populous in the CMZ (Messineo et al. 2002, 2020; Li et al. 2010; Borkar et al. 2020). As a result, the H¹³CN data is contaminated by sporadic SiO masers. This is most evident in the Galactic longitude-velocity map in Figure 10 where the l - V_{LSR} mask is not applied. The

other maps of H¹³CN presented in this paper have had the l - V_{LSR} mask applied to them, and therefore many, but not all, of the SiO masers have been excluded.

- The SO (2_2-1_1) and HC¹⁵N ($1-0$) lines are close in rest frequency, and therefore contaminate each other in the Galactic longitude-velocity maps in Figure 10 where both lines can be clearly seen in the plot of the other line. To separate emission of the two lines, for SO (2_2-1_1), the maximum V_{LSR} boundaries of the l - V_{LSR} mask at $l = 0.9^\circ$ and -0.6° are adjusted to 150 and 50 $km\ s^{-1}$, respectively, whereas for HC¹⁵N ($1-0$), the minimum V_{LSR} boundaries of the l - V_{LSR} mask are 0 and -100 $km\ s^{-1}$, respectively. The contamination is alleviated but not fully removed. Users of the data are encouraged to design a more sophisticated mask to effectively separate the two lines.

- The H¹³CO⁺ ($1-0$) and SiO ($2-1$) lines are also close in rest frequency. In Figure 10, the SiO emission appears at the blue-shifted

velocities ($< -200 \text{ km s}^{-1}$) in the plot of H^{13}CO^+ . To get rid of the SiO contamination, the minimum V_{LSR} boundaries of the l - V_{LSR} mask are -50 and -150 km s^{-1} , respectively. Again, users of the data could design their own masks to more effectively remove the SiO contamination.

- The $\text{HN}^{13}\text{C}(1-0)$ line is on the high-frequency edge of the 12-m SPW 27, and therefore its cube is truncated at the blue-shifted side, as shown in Figure 10.

4 DISCUSSION

4.1 Morphological correlations between the continuum and the molecular emission

The 3 mm continuum emission of the survey has been presented in Paper II, in which we have combined data from the ALMA 12-m array, the 7-m array, and the Green Bank Telescope MUSTANG-2 bolometer camera. Within the massive molecular clouds in the CMZ, e.g., Sgr B2, Sgr C, the 20 km s^{-1} cloud, and the Dust Ridge clouds, the continuum mostly originates from thermal dust emission in dense molecular gas, and therefore it is a good tracer of dense cores. Outside of the massive molecular clouds, the continuum could also stem from free-free emission in HII regions or synchrotron emission.

The 2-dimensional (2-D) Pearson correlation coefficient (ρ) is a useful reference to reveal morphological similarities between different tracers and help understand their potential physical and chemical origins (e.g., Lu et al. 2017; Callanan et al. 2023). In Figure 12, we present 2-D correlations between the continuum image and the integrated brightness images of all the major molecular lines covered in the ACES SPWs, including the six lines in 12-m SPWs 25 and 27. We calculate ρ using the `corrcoef` function in NumPy. The resulting values of ρ are between -1 and 1 , with -1 being anti-correlated, 0 being not correlated at all, and 1 being correlated. Note that we present results with and without considering the Sgr B2 and Sgr A regions, where the continuum and line emissions are brightest among the ACES fields and therefore could bias the correlations.

Among the 14 lines, the radio recombination line $\text{H}40\alpha$ shows the highest correlation coefficient with the continuum. The commonly used dense gas tracers for the Galactic disk and external galaxies, including $\text{HNCO}(4-3)$, $\text{HCO}^+(1-0)$, and $\text{CS}(2-1)$, turn out to show only weak correlations with the continuum, probably because of a combined effect of the continuum not well tracing dense gas (e.g., free-free or synchrotron contamination) and the lines not correlating with dense gas (e.g., potentially optically thick line emission, enhancement of line emission by shocks). In the following, we only focus on the six lines covered by the 12-m SPWs 25 and 27, and leave in-depth discussions to future works.

When Sgr B2 and Sgr A are included in the calculation, the $\text{SO}(2_2-1_1)$ line covered by the 12-m SPW 25 has the second highest correlation coefficient with the continuum ($\rho = 0.72$) after $\text{H}40\alpha$, as shown in Figure 12 top panel. However, once Sgr B2 is excluded, $\text{SO}(2_2-1_1)$ only shows a weak correlation with the continuum ($\rho = 0.43$; see Figure 12 bottom). We also find a strong correlation between SO and the continuum within the Sgr B2 region ($\rho = 0.71$). Excluding Sgr A makes no difference to the correlation between the two.

Therefore, it is likely that the correlation between $\text{SO}(2_2-1_1)$ and the continuum is biased by the bright emission in Sgr B2. The $\text{SO}(2_2-1_1)$ in Sgr B2 has been mapped with single-dish observations by Jones et al. (2008), who noted that this line presents compact peaks near the two hot cores, Sgr B2(M) and (N). This morphological similarity may be attributed to the fact that the $\text{SO}(2_2-1_1)$ transition

has the lowest Einstein coefficient and the highest upper level energy among the six lines (Table 1), and therefore can be more easily excited in environments such as the hot cores in Sgr B2. SO has been suggested to be enhanced by slow shocks ($\lesssim 20 \text{ km s}^{-1}$) that prevail in the CMZ (Lis et al. 2001; Lu et al. 2017; Callanan et al. 2023). It has been found to trace both dense molecular gas and shocks in other galactic nuclei (Bouvier et al. 2024); however, it is not clear if the SO emission actually traces unresolved protostellar outflows or shock-related filaments inside the dense gas (e.g., Lu et al. 2021; Busch et al. 2024; Yang et al. 2025). A combined analysis with other SO transitions as well as its isotopologue lines (e.g., $\text{SO}(2_3-1_2)$, $^{33}\text{SO}(2_3-1_2)$; see Paper V) covered in the other SPWs of the ACES observations will be helpful for understanding the excitation condition of this molecule.

The $\text{HC}^{15}\text{N}(1-0)$ line has a weak correlation with the continuum, regardless of whether or not Sgr B2 and Sgr A are included in the analysis ($\rho = 0.39$ or 0.44). Its low peak brightness temperature in Figure 4, which is much lower than the typical kinetic temperature of 50 – 100 K (Ginsburg et al. 2016b; Krieger et al. 2017), suggests that the line is optically thin in most of the surveyed area. Therefore, the HC^{15}N line could be a good tracer of dense gas in massive molecular clouds in this environment, even in Sgr B2. Studies comparing the line emission and dense gas mass derived from *Herschel* multi-wavelength observations can be carried out to confirm the robustness of this trend (e.g., Mills & Battersby 2017).

The remaining four lines, including $\text{SiO}(2-1)$, $\text{H}^{13}\text{CO}^+(1-0)$, $\text{H}^{13}\text{CN}(1-0)$, and $\text{HN}^{13}\text{C}(1-0)$, all have spatially diffuse and often filamentary emission across the whole CMZ. As such, their correlation coefficients with the spatially compact continuum are $\lesssim 0.3$ when Sgr B2 and Sgr A are included, suggesting weak to no correlation. When Sgr B2 and Sgr A are excluded, their ρ remains at ~ 0.3 – 0.4 , suggesting weak correlations. Between the four lines, however, we find strong correlations with $\rho > 0.6$, which do not change when Sgr B2 and Sgr A are excluded in the correlation analysis. This result reflects their similarity in morphology. Indeed, the four lines have been found to be widespread in the CMZ in previous single dish observations (e.g., Martín-Pintado et al. 1997; Riquelme et al. 2010b; Jones et al. 2012; Tanaka et al. 2018). The SiO emission is likely related to shocks in this environment (Martín-Pintado et al. 1997; Liu et al. 2013; Lu et al. 2017; Coutens et al. 2017). The H^{13}CO^+ , H^{13}CN , and HN^{13}C lines are usually used to trace molecular clouds given their high critical densities and their lower opacity with respect to their main isotopologues, HCO^+ , HCN , and HNC (Jones et al. 2012). With the higher angular resolution of ACES, however, one could find that the three lines present ubiquitous filamentary structures across the CMZ, one of which can be clearly seen in the Sgr B1 region, a feature similar to that seen in SiO . The filamentary structures could be related to active shock activities in the CMZ, whose origin is still under debate (e.g., expansion of HII regions or supernova remnants: Inutsuka 2021; Henshaw et al. 2022; cloud-cloud collision, tidal force, or shear: Kruijssen et al. 2014; C. Battersby et al. 2025 submitted). This may suggest that the formation of the three isotopologues is related to shocks, e.g., they might be synthesized in the gas phase in post-shock regions. In such regions, shocks sputter SiO from dust grains and compress the gas to densities above 10^5 cm^{-3} (Schilke et al. 1997; Bachiller & Pérez Gutiérrez 1997), which are consistent with the critical densities of the three isotopologue lines.

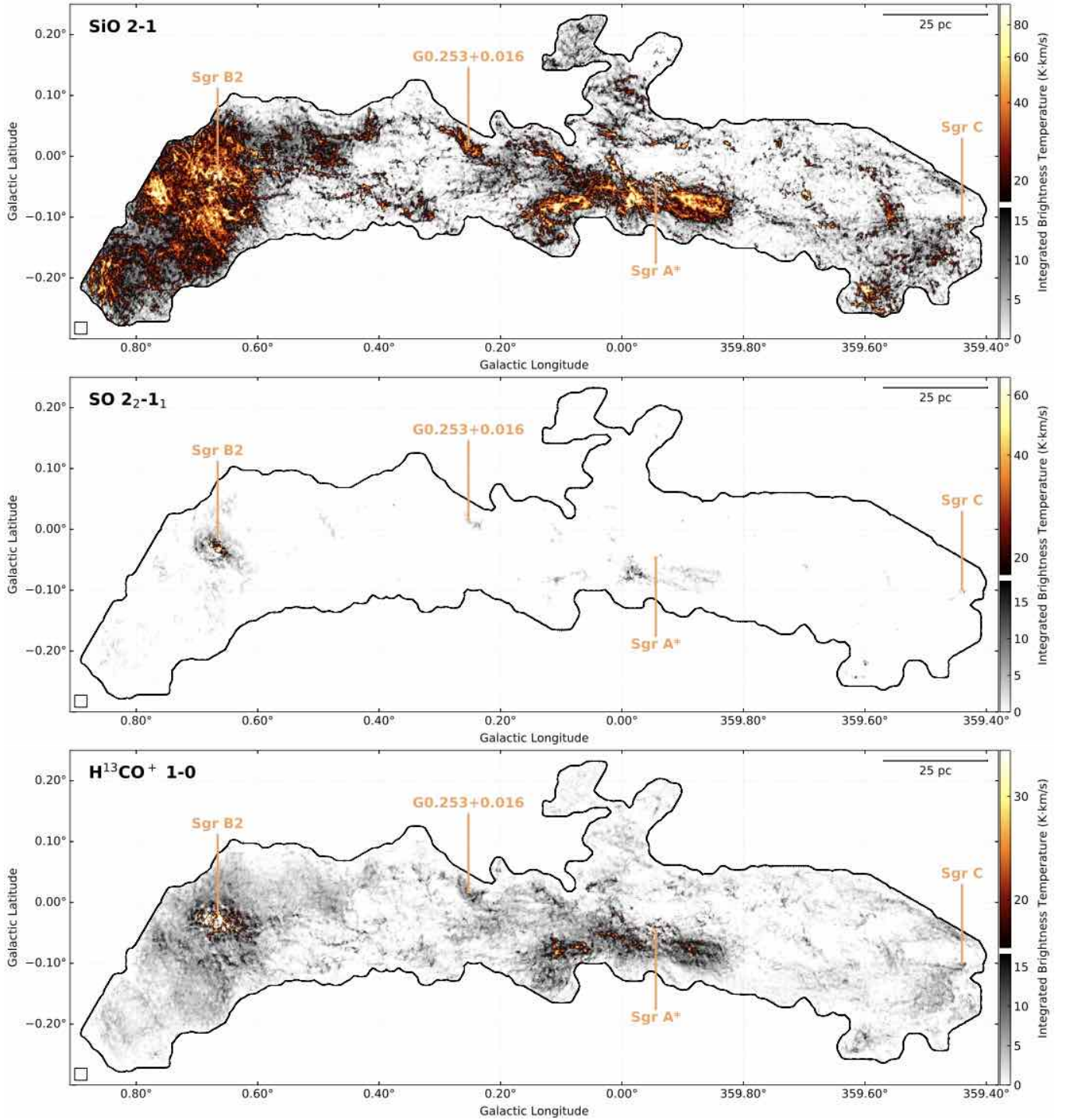


Figure 2. Integrated brightness temperature maps of SiO (2–1), SO (2_2-1_1), and H^{13}CO^+ (1–0). The two-piece colour bars are a combination of a linear scale between 0 and approximately 5σ and a logarithmic scale above approximately 5σ up to the 99.9 percentile of the data.

4.2 Line ratios between H^{13}CN , HN^{13}C , and HC^{15}N

The relative intensities or densities of H^{13}CN and HC^{15}N with respect to that of HCN are related to the $^{12}\text{C}/^{13}\text{C}$ and $^{14}\text{N}/^{15}\text{N}$ isotope abundance ratios, respectively. Lines of the main isotopologue $\text{H}^{12}\text{C}^{14}\text{N}$ are not covered in the ACES observations. Nonetheless, the ratio between the H^{13}CN and HC^{15}N lines is still informative. Previous observations toward nearby clouds have found that the integrated

brightness temperature ratio between H^{13}CN and HC^{15}N can vary between ~ 3 and ~ 10 (Ikeda et al. 2002). This translates to a ratio of their densities in the same range if one assumes the same excitation temperature and optically thin emission for both lines.

We present the ratio of integrated brightness temperatures of HC^{15}N (1–0) and H^{13}CN (1–0) in the ACES data in Figure 13. Note that we do not derive the ratio of peak brightness temperatures

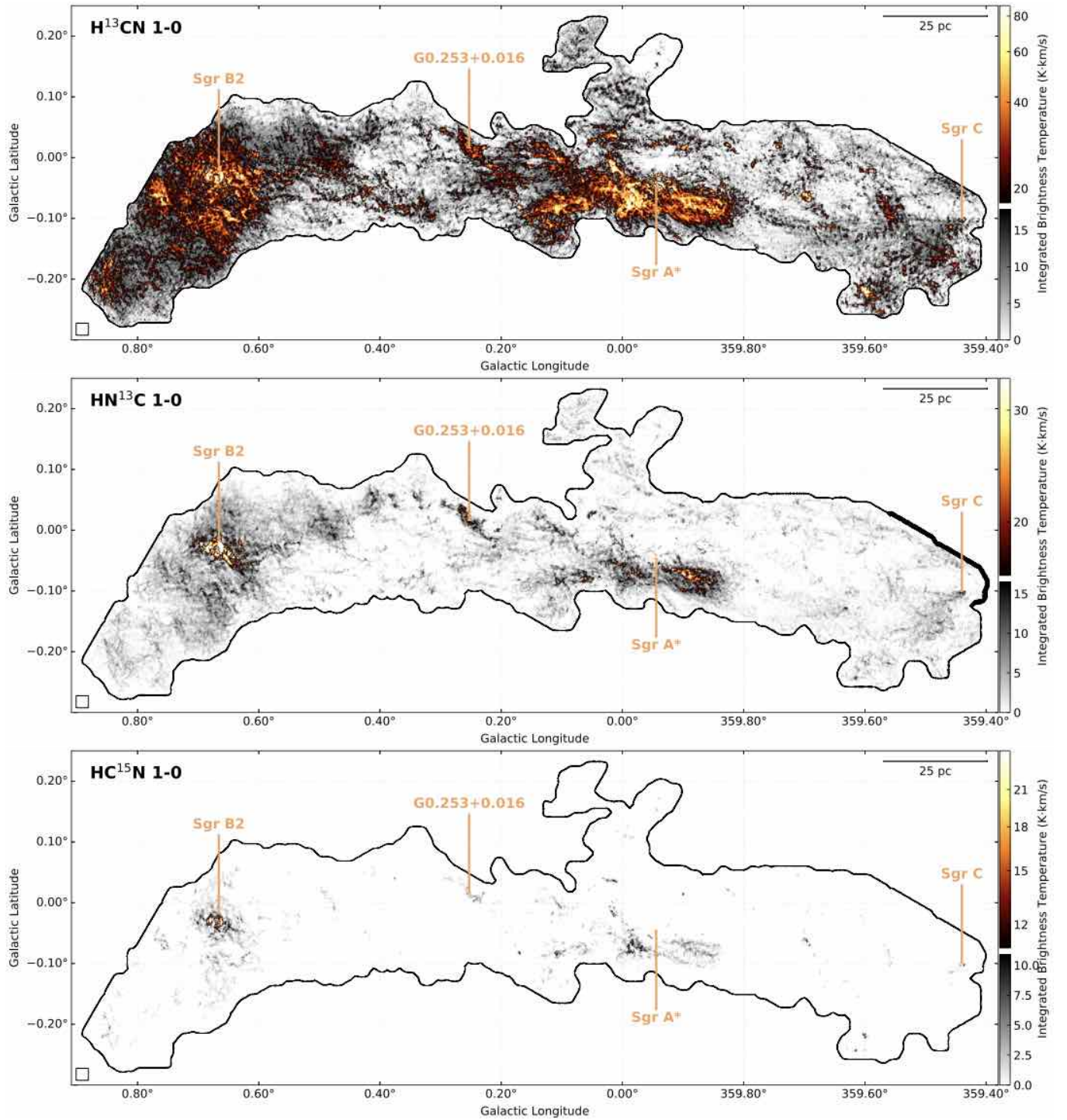


Figure 3. Integrated brightness temperature maps of H^{13}CN (1–0), HN^{13}C (1–0), and HC^{15}N (1–0). The two-piece colour bars are a combination of a linear scale between 0 and approximately 5σ and a logarithmic scale above approximately 5σ up to the 99.9 percentile of the data.

of the two lines, because their spectral profiles are not the same and therefore their peaks do not align in the velocity axis. Comparing their integrated brightness temperatures has its own problem, e.g., the line widths of the two lines could be different. Nonetheless, we use the ratio in Figure 13 as a starting point to demonstrate what could be learned from these two lines. Following the same assump-

tions in Ikeda et al. (2002), the ratio is related to the compound isotope abundance ratio $(^{12}\text{C}/^{13}\text{C})(^{14}\text{N}/^{15}\text{N})$.

If the $^{12}\text{C}/^{13}\text{C}$ isotope ratio could be estimated, e.g., from other isotopologue pairs (H^{13}CO^+ and HCO^+ ; for the latter line, see Paper III), then we can decouple the nitrogen isotopic ratio $^{14}\text{N}/^{15}\text{N}$ from the compound ratio derived from HC^{15}N and H^{13}CN . The nitrogen isotopic ratio has been shown to vary significantly in different

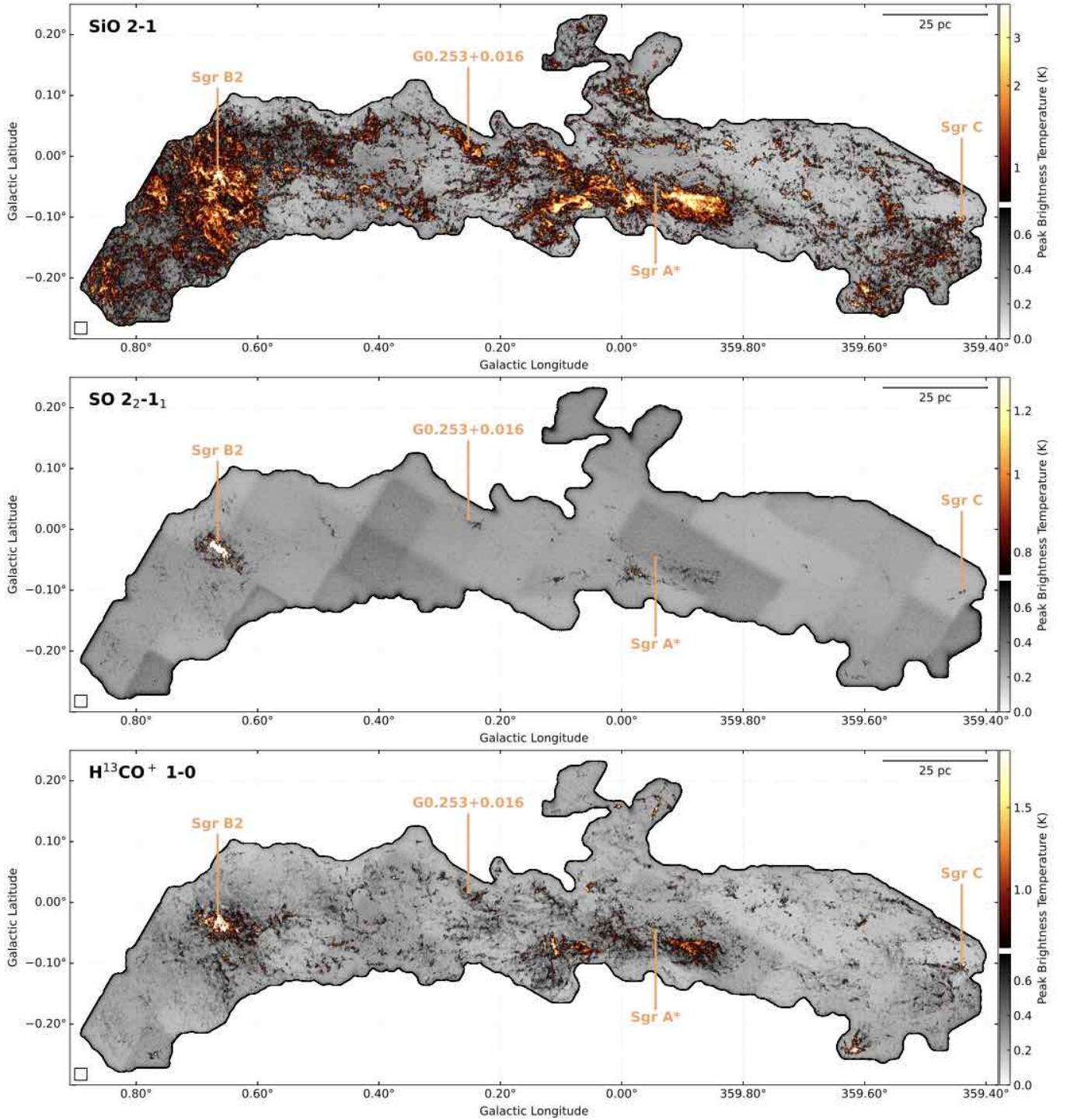


Figure 4. Peak brightness temperature maps of SiO (2–1), SO (2_2-1_1), and H^{13}CO^+ (1–0). The two-piece colour bars are a combination of a linear scale between 0 and approximately 5σ and a logarithmic scale above approximately 5σ up to the 99.9 percentile of the data.

environments (Fontani et al. 2015; Colzi et al. 2018), and is an important constraint in astrochemical models and in simulations of the evolution of the Galactic stellar population.

The HN^{13}C molecule is an isotopomer of H^{13}CN , and their line ratio is suggested to be anti-correlated with the gas temperature and therefore a potential gas thermometer (e.g., Hirota et al. 1998; Jin et al. 2015; Pazukhin et al. 2022). Both lines are optically thinner

than their respective main isotopologue HNC and HCN, whose ratio has been shown to be correlated with the gas temperature (Graninger et al. 2014; Hacar et al. 2020) but may be biased when the emission is optically thick. Therefore, the $\text{HN}^{13}\text{C}/\text{H}^{13}\text{CN}$ line ratio is particularly of interest in the CMZ, where the HCN emission becomes optically thick (Jones et al. 2012).

As shown in Figure 13, the $\text{HN}^{13}\text{C}/\text{H}^{13}\text{CN}$ line ratio varies be-

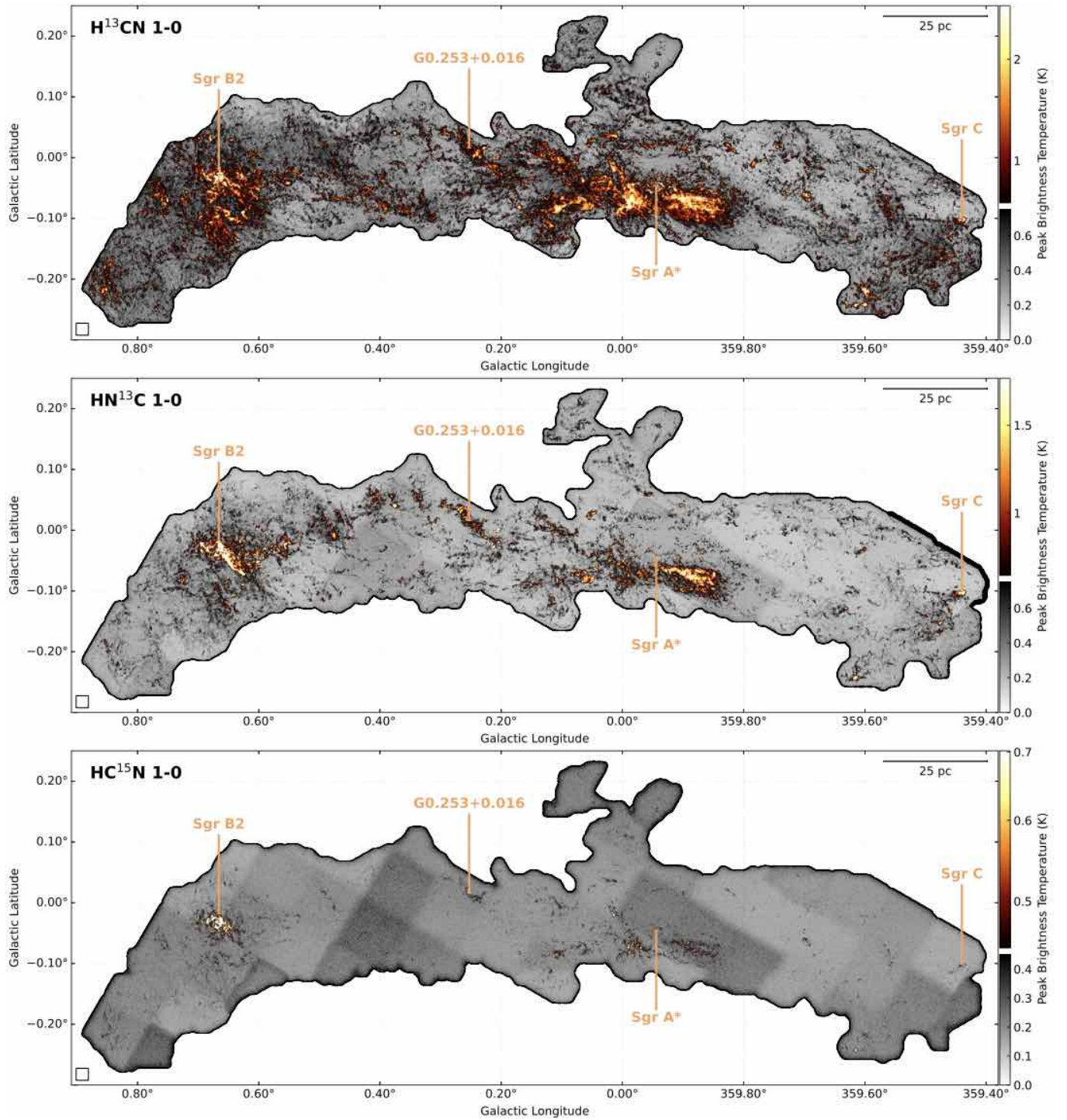


Figure 5. Peak brightness temperature maps of H^{13}CN (1–0), HN^{13}C (1–0), and HC^{15}N (1–0). The two-piece colour bars are a combination of a linear scale between 0 and approximately 5σ and a logarithmic scale above approximately 5σ up to the 99.9 percentile of the data.

tween ~ 0.01 and >10 (truncated in the plot). The line ratio shows a possible increasing trend towards the interiors of molecular clouds including Sgr B2, the Brick, and the 20 km s^{-1} cloud. Clouds in the CMZ are known to be externally heated (e.g., [Molinari et al. 2011](#); [Rathborne et al. 2014a](#)). Therefore, the anti-correlation between the line ratio and temperature could still hold for the CMZ. With the high resolution of the ACES observations, one will be able to explore the

$\text{HN}^{13}\text{C}/\text{H}^{13}\text{CN}$ line ratio and the gas temperature derived from e.g., multiple NH_3 lines across various environments in the CMZ. This will help sort out the impact of other factors on the ratio such as the ultraviolet radiation ([Santa-Maria et al. 2023](#); [Harada et al. 2024](#)) and calibrate this ratio as a gas thermometer, which then can be applied to studies of external galaxies (e.g., [Behrens et al. 2022](#); [Harada et al. 2024](#)).

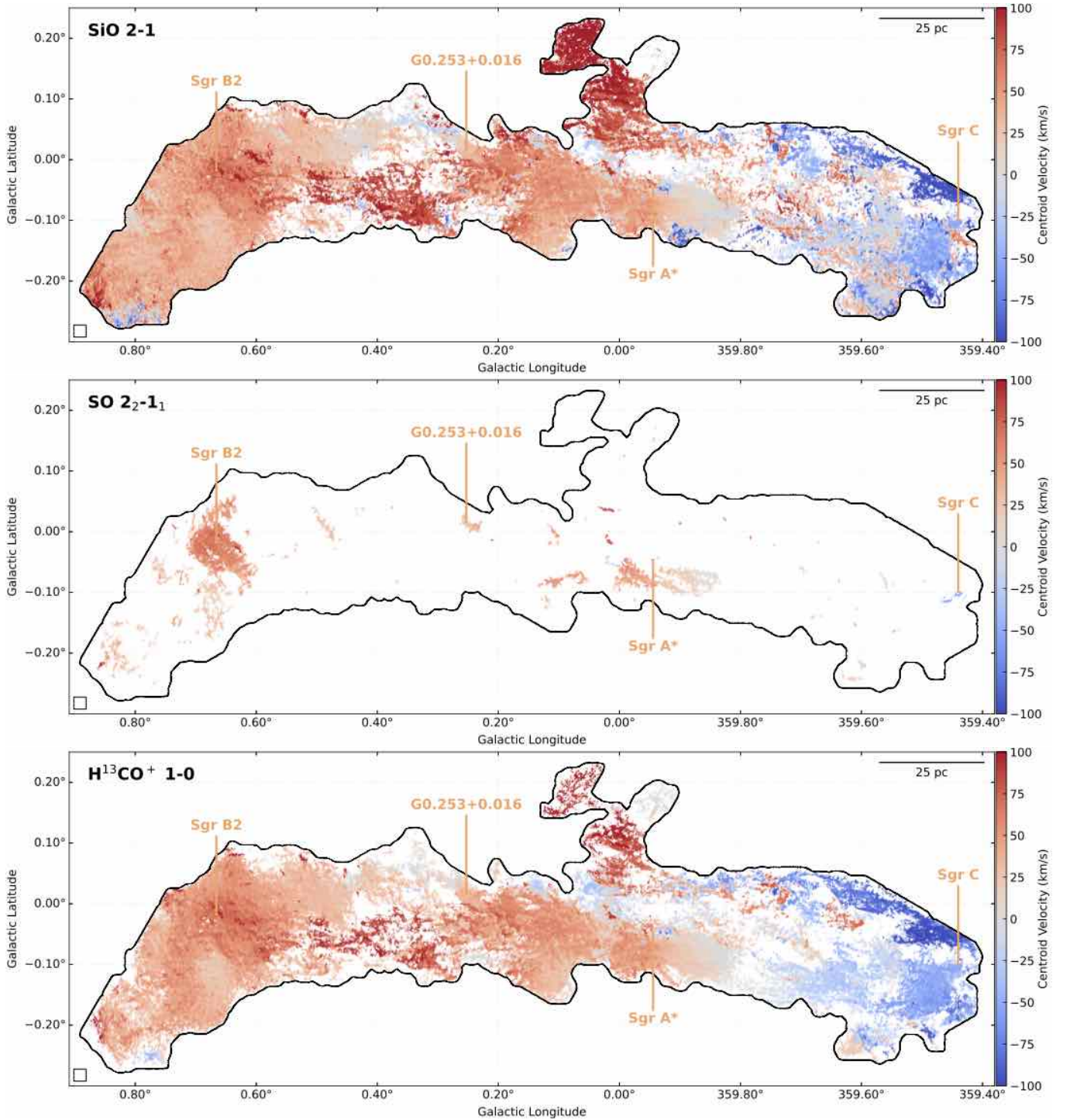


Figure 6. Centroid velocity maps of SiO (2–1), SO (2_2-1_1), and H^{13}CO^+ (1–0). All the colour bars are linear and truncated between -100 and 100 km s^{-1} to highlight the velocity structures.

Finally, in [Figure 13](#) we also present the line ratio map between H^{13}CO^+ (1–0) and HCO^+ (1–0), the latter of which is released in [Paper III](#). This ratio can be used as a metric of the $^{12}\text{C}/^{13}\text{C}$ isotope ratio, although HCO^+ likely becomes optically thick toward dense molecular clouds. As such, peaks in the bottom panel of, e.g., towards Sgr B2, may not necessarily suggest high $^{12}\text{C}/^{13}\text{C}$ isotope ratios, but

simply optically thick HCO^+ emission. In-depth analysis of this ratio is beyond the scope of this paper.

4.3 Other interesting features in the data

The maps in [Figures 2–7](#) reveal prominent morphological features in the CMZ, including rings, filaments, and clumpy clouds. Here we

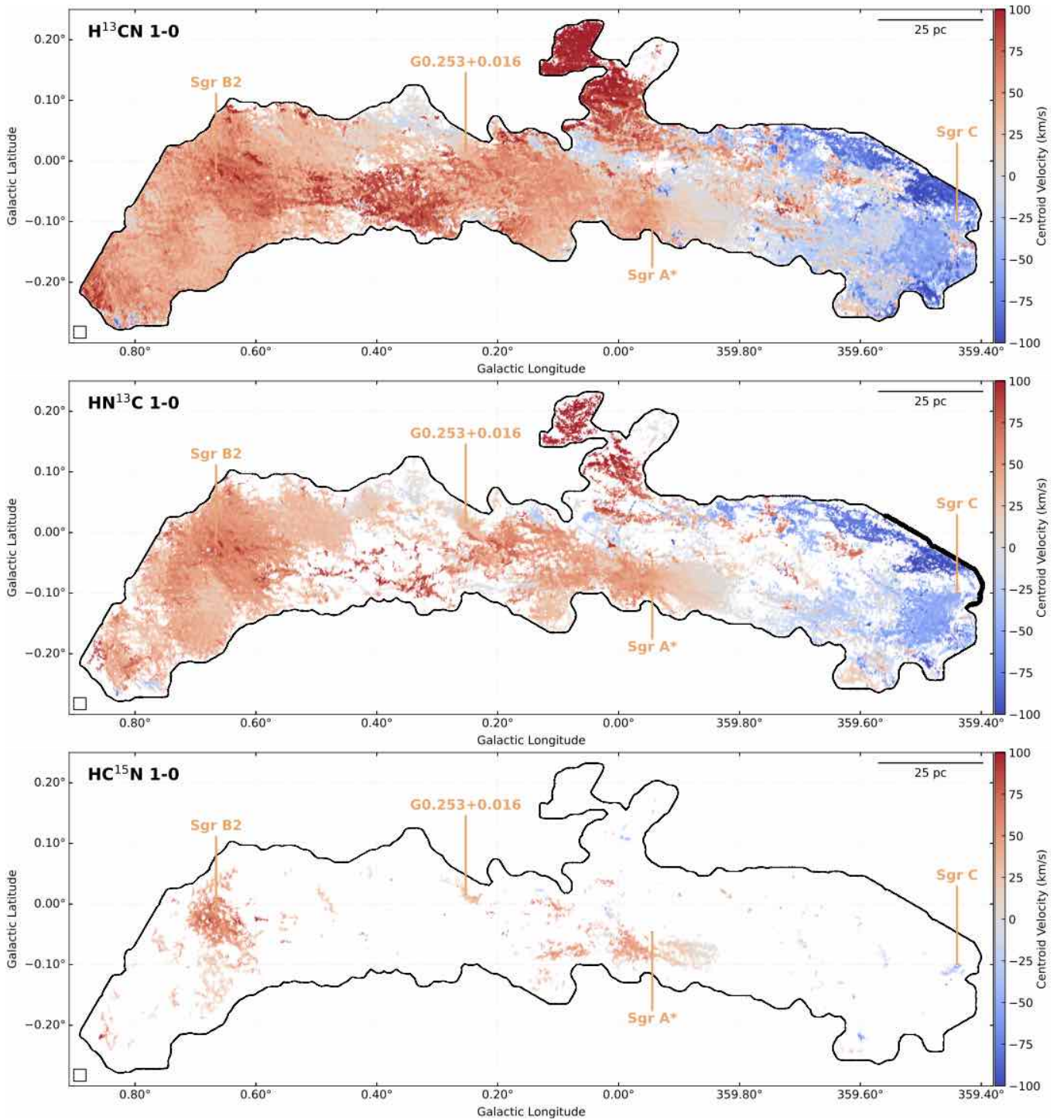


Figure 7. Centroid velocity maps of H^{13}CN (1–0), HN^{13}C (1–0), and HC^{15}N (1–0). All the colour bars are linear and truncated between -100 and 100 km s^{-1} to highlight the velocity structures.

highlight a few features of interest, and leave detailed discussions to science papers that are currently being prepared by the ACES team.

Nonhebel et al. (2024) have reported a detailed study of the M0.8–0.2 ring using the ACES data, which can be seen in the maps of SiO, H^{13}CN , H^{13}CO^+ , and HN^{13}C . The molecular line data are used for constraining the kinematics and energetics of the ring. There are numerous other ring-like structures of different angular scales in

the data, which might be related to supernova remnants or HII regions (e.g., ‘atolls’ in Hatchfield et al. 2024). A catalog of such objects will be valuable for studying the star formation history of the CMZ.

Filamentary structures at spatial scales of 0.1 pc to $\geq 10 \text{ pc}$ are known to be ubiquitous in molecular line emission in the CMZ (e.g., Bally et al. 2014; Johnston et al. 2014; Henshaw et al. 2019; Wallace et al. 2022; Yang et al. 2025). A large population of filaments

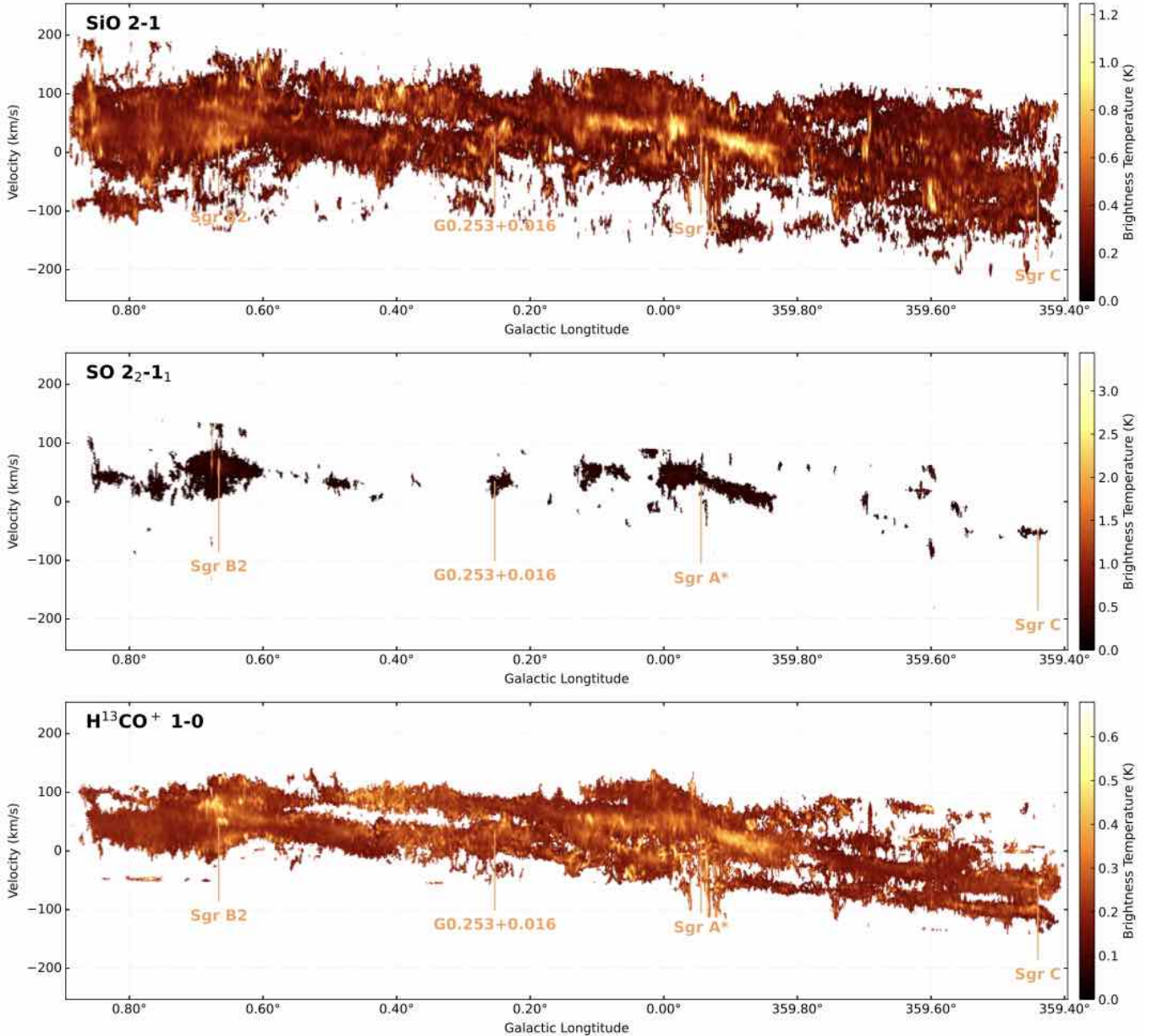


Figure 8. Position-velocity diagrams of SiO (2–1), SO (2₂–1₁), and H¹³CO⁺ (1–0). Here the intensities are the mean values of the cut along the Galactic latitude. The velocities are truncated by the l - V_{LSR} mask specified in Section 3.2.

are revealed in the molecular line emission presented in Section 3, particularly towards the Sgr B1 region between Galactic longitudes of 0°20′–0°40′ and latitudes of 0°–0°5′, which may trace the photo-dissociation region between the young massive star cluster Sgr B1 and the surrounding molecular gas (Simpson et al. 2018, 2021). The exact nature of the filaments, which could be diverse in spite of their similar morphologies, is yet to be explored with the ACES data (e.g., C. Battersby et al. 2026 submitted).

5 CONCLUSIONS

In this paper, we have presented an overview of spectral line data of the two intermediate-width spectral windows from the ACES Large

Program, with a focus on the six bright lines including SiO (2–1), SO (2₂–1₁), H¹³CO⁺ (1–0), H¹³CN (1–0), HN¹³C (1–0), and HC¹⁵N (1–0). We present the integrated brightness temperature, the peak brightness temperature, the centroid velocity, and the position-velocity diagrams along the Galactic longitude of the six lines. The data products are released along with the paper.

In addition, we showcase potential science that could be done with the data, including morphological correlations between the 3 mm continuum (Paper II) and the spectral line emissions (Paper III; Paper V, and this work) to understand the excitation conditions and chemical properties of the molecules, line ratios between isotopologues and isomers to estimate the isotope abundance ratio, and other features in the data such as rings and filaments. We leave in-

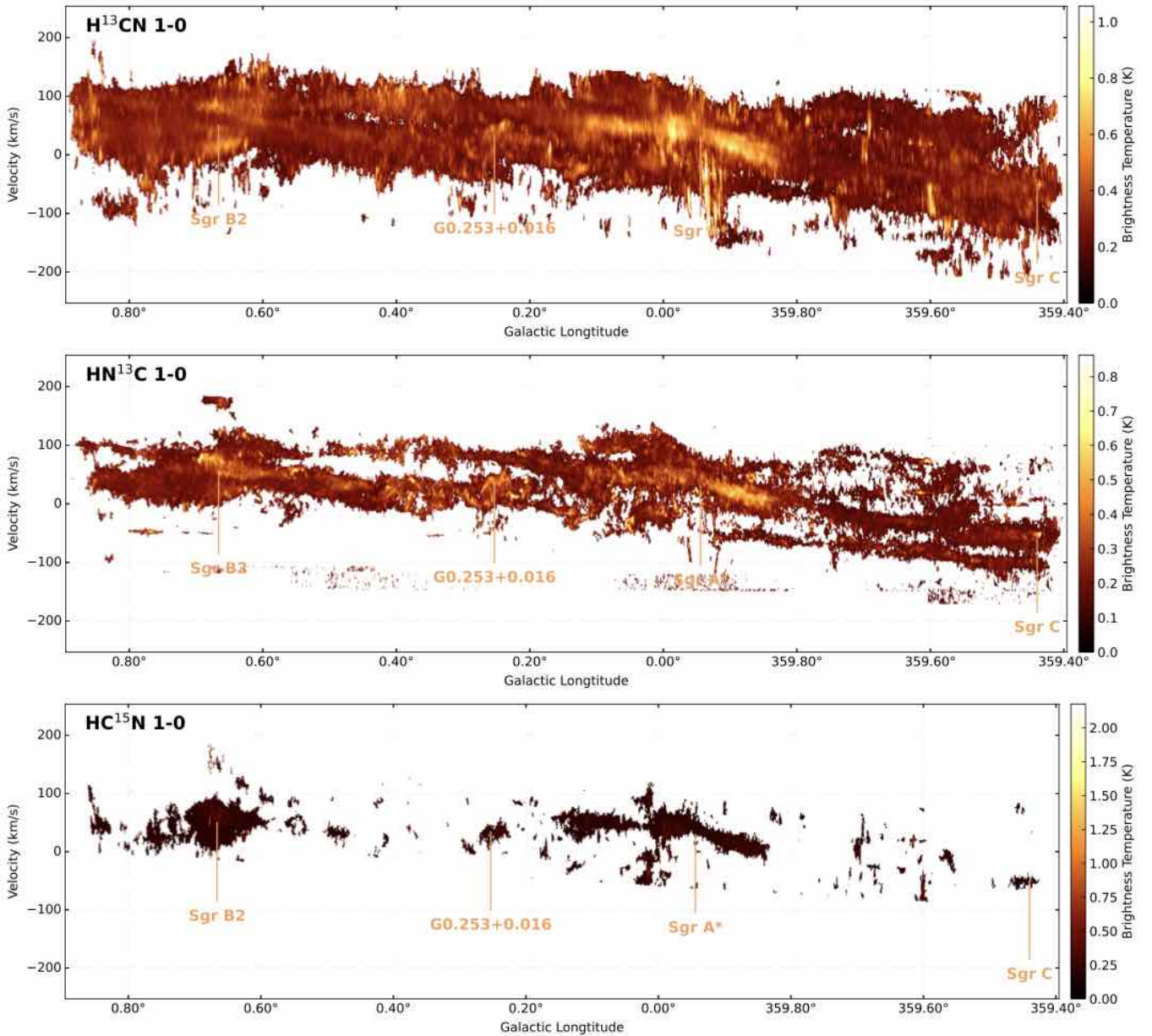


Figure 9. Position-velocity diagrams of H^{13}CN (1–0), HN^{13}C (1–0), and HC^{15}N (1–0). Here the intensities are the mean values of the cut along the Galactic latitude. The velocities are truncated by the l - V_{LSR} mask specified in Section 3.2.

depth discussions of these topics to follow-up papers in the ACES series and to users of the data.

ACKNOWLEDGEMENTS

The paper was instigated and led by the ACES data reduction working group, which is coordinated by Adam Ginsburg, Daniel Walker, and Ashley Barnes, and includes (alphabetically) Nazar Budaiev, Laura Colzi, Claire Cooke, Savannah Gramze, Pei-Ying Hsieh, Desmond Jeff, Xing Lu, Jaime Pineda, Marc Pound, Álvaro Sánchez-Monge, and Qizhou Zhang. ACES is led by Principal Investigator Steven Longmore, together with co-PIs and the management team, John Bally, Ashley Barnes, Cara Battersby, Laura Colzi, Adam Gins-

burg, Jonathan Henshaw, Paul Ho, Izaskun Jiménez-Serra, Elisabeth Mills, Maya Petkova, Mattia Sormani, Robin Tress, Daniel Walker, and Jennifer Wallace. The ACES proposal was led by Principal Investigator Steven Longmore, together with co-PIs John Bally, Cara Battersby, Adam Ginsburg, Jonathan Henshaw, Paul Ho, J. M. Diederik Kruijssen, Izaskun Jiménez-Serra, and Elisabeth Mills. The remaining coauthors comprise the ACES team, and its members contributed to the proposal, data analysis, idea development, and/or reading and commenting on the manuscript. X.L. acknowledges support from the Strategic Priority Research Program of the Chinese Academy of Sciences (CAS) Grant No. XDB0800300, the National Key R&D Program of China (No. 2022YFA1603101), the National Natural Science Foundation of China (NSFC) through grant Nos. 12273090 and 12322305, the Natural Science Founda-

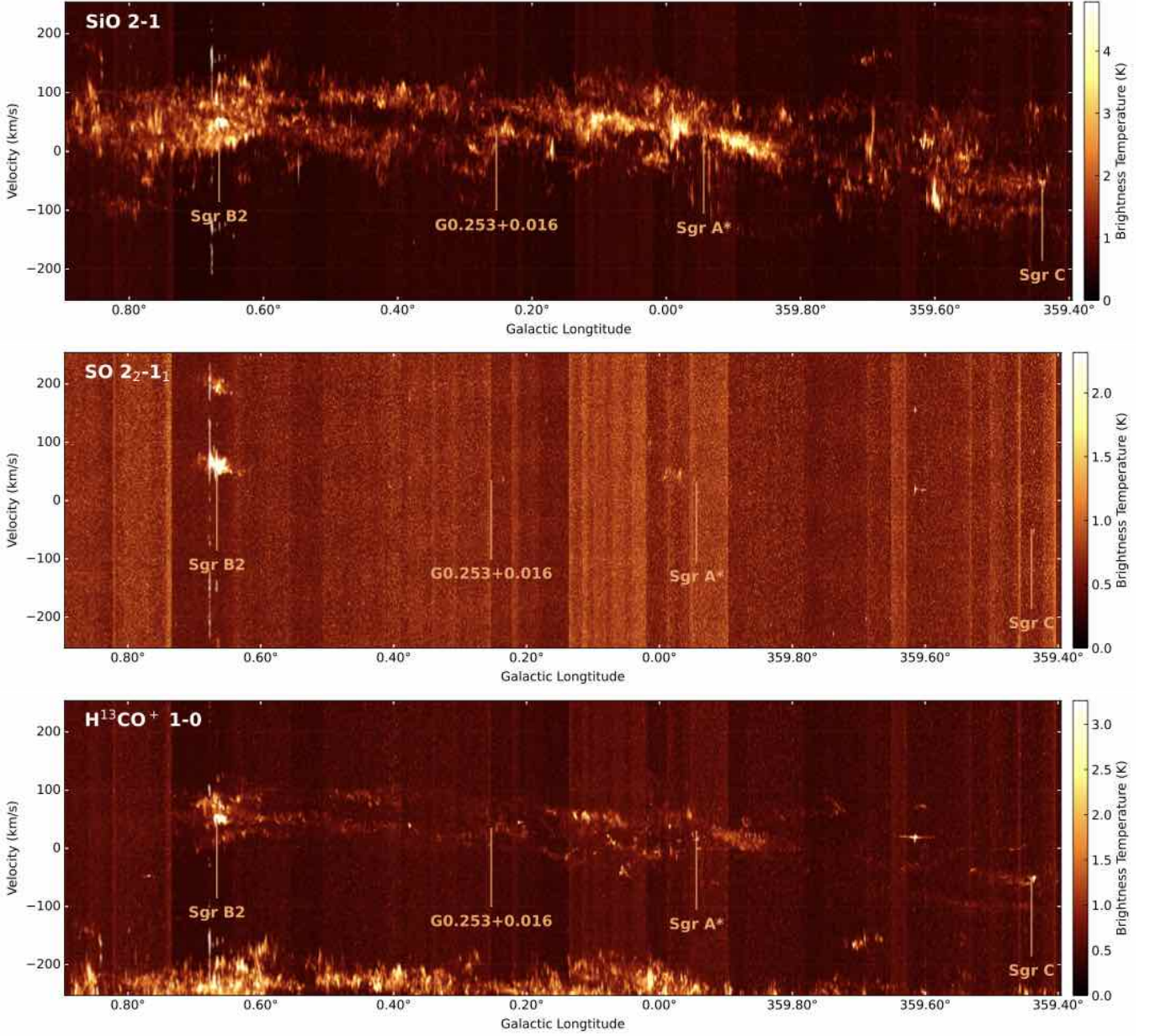


Figure 10. Position-velocity diagrams of SiO (2–1), SO (2₂–1₁), and H¹³CO⁺ (1–0). Here the intensities are the maximum values of the cut along the Galactic latitude, without the $I-V_{LSR}$ mask.

tion of Shanghai (No. 23ZR1482100), and the CAS “Light of West China” Program No. xzbzgz-zdsys-202212. D.L.W gratefully acknowledges support from the UK ALMA Regional Centre (ARC) Node, which is supported by the Science and Technology Facilities Council [grant numbers ST/Y004108/1 and ST/T001488/1]. R.F. acknowledges support from the grants PID2023-146295NB-I00, and from the Severo Ochoa grant CEX2021-001131-S funded by MCIN/AEI/10.13039/501100011033 and by “European Union NextGenerationEU/PRTR”. COOL Research DAO (Chevance et al. 2025) is a Decentralized Autonomous Organization supporting research in astrophysics aimed at uncovering our cosmic origins. I.J.-S., L.C., and V.M.R. acknowledge support from the grant PID2022-136814NB-I00 by the Spanish Ministry of Science, Innovation and Universities/State Agency of Research MICIU/AEI/10.13039/501100011033

and by ERDF, UE. I.J.-S. also acknowledges the ERC Consolidator grant OPENS (project number 101125858) funded by the European Union. V.M.R. also acknowledges the grant RYC2020-029387-I funded by MICIU/AEI/10.13039/501100011033 and by “ESF, Investing in your future”, and from the Consejo Superior de Investigaciones Científicas (CSIC) and the Centro de Astrobiología (CAB) through the project 20225AT015 (Proyectos intramurales especiales del CSIC); and from the grant CNS2023-144464 funded by MICIU/AEI/10.13039/501100011033 and by “European Union NextGenerationEU/PRTR. The authors acknowledge UFIT Research Computing for providing computational resources and support that have contributed to the research results reported in this publication. A.G acknowledges support from the NSF under grants CAREER 2142300, AAG 2008101, and particularly AAG 2206511 that

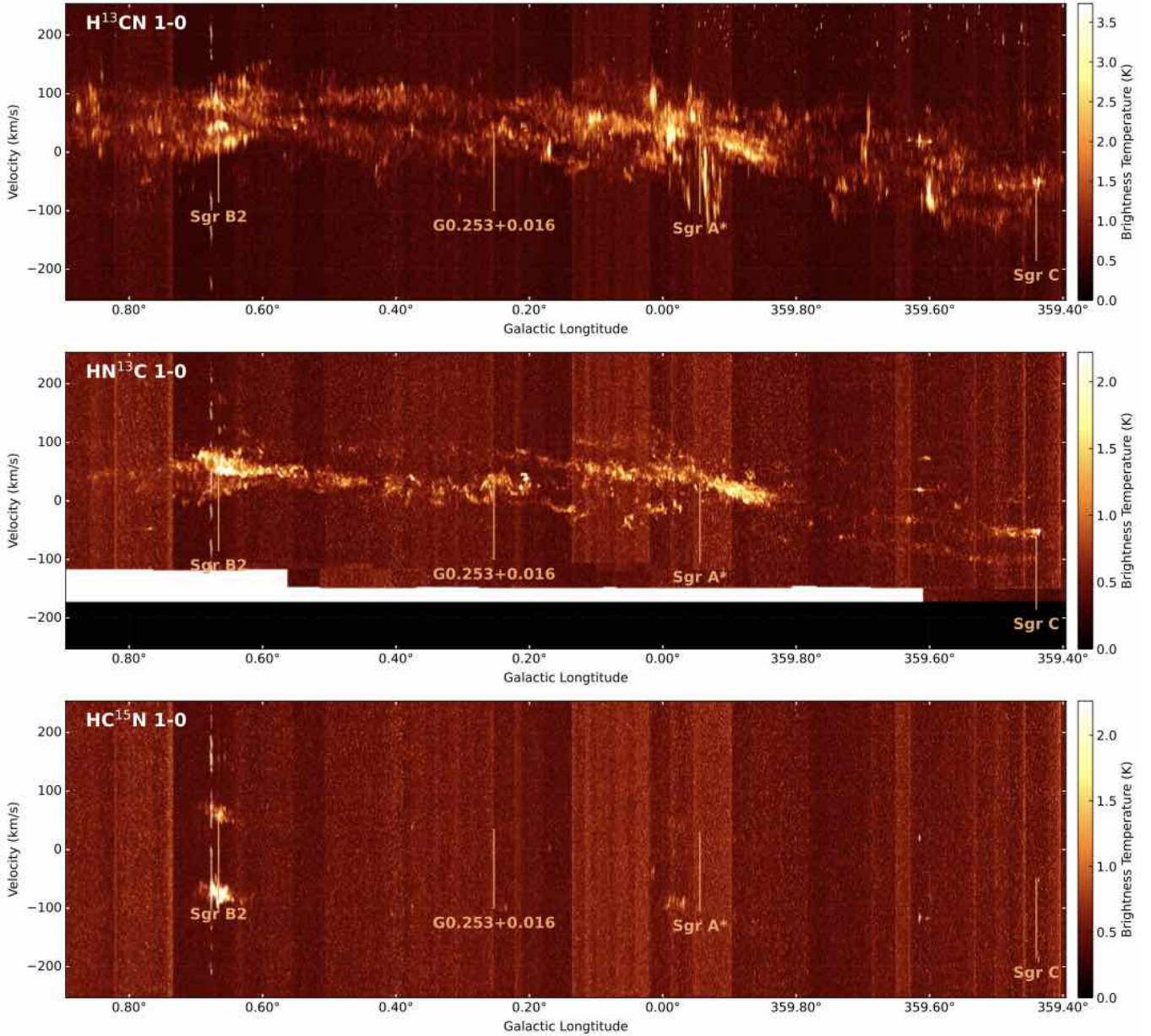


Figure 11. Position-velocity diagrams of H^{13}CN (1–0), HN^{13}C (1–0), and HC^{15}N (1–0). Here the intensities are the maximum values of the cut along the Galactic latitude, without the l - V_{LSR} mask.

supports the ACES large program. P.-Y. H. acknowledges support from the ADC. Data analysis was in part carried out on the Multi-wavelength Data Analysis System operated by the Astronomy Data Center (ADC), National Astronomical Observatory of Japan. E.A.C. Mills gratefully acknowledges funding from the National Science Foundation under Award Nos. 1813765, 2115428, 2206509, and CAREER 2339670. M.G.S.-M. acknowledges support from the NSF under grant CAREER 2142300. M.G.S.-M. also thanks the Spanish MICINN for funding support under grant PID2023-146667NB-I00. A.S.-M. acknowledges support from the RyC2021-032892-I grant funded by MCIN/AEI/10.13039/501100011033 and by the European Union ‘Next GenerationEU’/PRTR, as well as the program Unidad de Excelencia María de Maeztu CEX2020-001058-M, and support from the PID2023-146675NB-I00 (MCI-AEI-FEDER,

UE). K.M.D acknowledges support from the European Research Council (ERC) Advanced Grant MOPPEX 833460.vii. Q.Z. gratefully acknowledges the support from the National Science Foundation under Award No. AST-2206512, and the Smithsonian Institute FY2024 Scholarly Studies Program. FHL acknowledges support from the ESO Studentship Programme, the Scatcherd European Scholarship of the University of Oxford, and the European Research Council’s starting grant ERC StG-101077573 (‘ISM-METALS’). C.F. acknowledges funding provided by the Australian Research Council (Discovery Projects DP230102280 and DP250101526), and the Australia-Germany Joint Research Cooperation Scheme (UA-DAAD). F. M acknowledges financial support from the School of Astronomy at the Institute for Research in Fundamental Sciences-IPM. J.K. is supported by the Royal Society under grant number

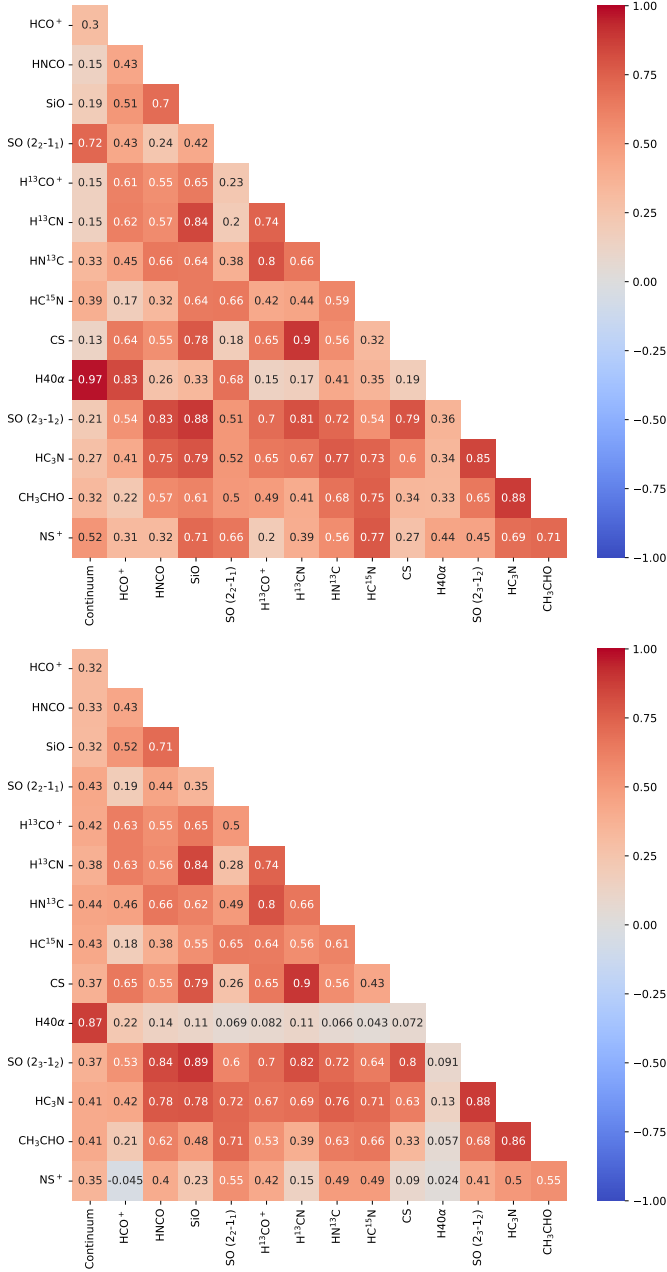


Figure 12. Top: 2-D correlation matrix between the continuum and integrated intensities of the six molecular line emission presented in this paper as well as eight lines in the other SPWs (Paper III; Paper V). All the pixels in the ACES mosaic fields are considered. Bottom: the same correlation matrix but with pixels in Sgr B2 and Sgr A masked out. The rectangular mask towards Sgr B2 is centered at (R.A., Dec.)=(17:47:20.14, $-28^{\circ}22'54''.66$), with a height of $26''.15$ and a height of $110''.08$. The square mask towards Sgr A is centered at (R.A., Dec.)=(17:45:40.14, $-29^{\circ}00'28''.24$), with a side length of $48''.64$.

RFERE\231132, as part of project URF\R1\211322. M.C. gratefully acknowledges funding from the DFG through an Emmy Noether Research Group (grant number CH2137/1-1). MCS acknowledges financial support from the European Research Council under the ERC Starting Grant “GalFlow” (grant 101116226) and from Fondazione Cariplo under the grant ERC attrattività n. 2023-3014. J.Wallace gratefully acknowledges funding from National Science Foundation under Award Nos. 2108938 and 2206510. F.N.-L. gratefully

acknowledges financial support from grant PID2024-162148NA-I00, funded by MCIN/AEI/10.13039/501100011033 and the European Regional Development Fund (ERDF) “A way of making Europe”, from the Ramón y Cajal programme (RYC2023-044924-I) funded by MCIN/AEI/10.13039/501100011033 and FSE+, and from the Severo Ochoa grant CEX2021-001131-S, funded by MCIN/AEI/10.13039/501100011033. C.B. gratefully acknowledges funding from National Science Foundation under Award Nos. 2108938, 2206510, and CAREER 2145689, as well as from the National Aeronautics and Space Administration through the Astrophysics Data Analysis Program under Award “3-D MC: Mapping Circumnuclear Molecular Clouds from X-ray to Radio,” Grant No. 80NSSC22K1125. S.Z. acknowledges support from the NAOJ ALMA Scientific Research Grant Code 2025-29B. This paper makes use of the following ALMA data: ADS/JAO.ALMA#2021.1.00172.L. ALMA is a partnership of ESO (representing its member states), NSF (USA) and NINS (Japan), together with NRC (Canada), NSTC and ASIAA (Taiwan), and KASI (Republic of Korea), in cooperation with the Republic of Chile. The Joint ALMA Observatory is operated by ESO, AUI/NRAO and NAOJ. The authors are grateful to the staff throughout the ALMA organisation, particularly those at the European ALMA Regional Centre, the Joint ALMA Observatory, and the UK ALMA Regional Centre Node, for their extensive support, which was essential to the success of this challenging Large Program. The authors thank the anonymous referee, whose feedback was critical for improving the clarity and utility of this paper.

SOFTWARE

The ACES pipeline is based on a number of open-source astronomy software packages, including *astropy* (Astropy Collaboration et al. 2013; Price-Whelan et al. 2018; Astropy Collaboration et al. 2022), *astroquery* (Ginsburg et al. 2019b), *spectral-cube* (Ginsburg et al. 2019a), *radio-beam* (Koch et al. 2025), *pvextractor* (Ginsburg et al. 2016a), *reproject* (Robitaille et al. 2020), *statcont* (Sánchez-Monge et al. 2018), *CASA* (CASA Team et al. 2022), *numpy* (Harris et al. 2020), and *matplotlib* (Hunter 2007). In addition, this paper made use of the following software packages: *CARTA* (Comrie et al. 2021) to visualise and analyse the data, and *APLpy* (Robitaille & Bressert 2012) and *seaborn* (Waskom 2021) to make plots.

DATA AVAILABILITY

All data products and associated documentation can be found at <https://almascience.org/alma-data/lp/aces>. To maximise usability and provide a single, comprehensive resource for users, we also provide an online, machine-readable megatable, which contains the full, detailed list of all data products released for the entire survey, including hyperlinks to the full files from the ALMA archive.

All code and data processing issues are available at the public GitHub repository here: https://github.com/ACES-CMZ/reduction_ACES.

The ACES data reduction was a gigantic monolithic work that was written up in 5 papers. If you use the ACES data, please cite the appropriate works, which includes Longmore & ACES Team (2026) and the data papers: continuum (Ginsburg & ACES Team 2026) and cubes in high-resolution (Walker & ACES Team 2026), medium-resolution (this work), and low-resolution (Hsieh & ACES

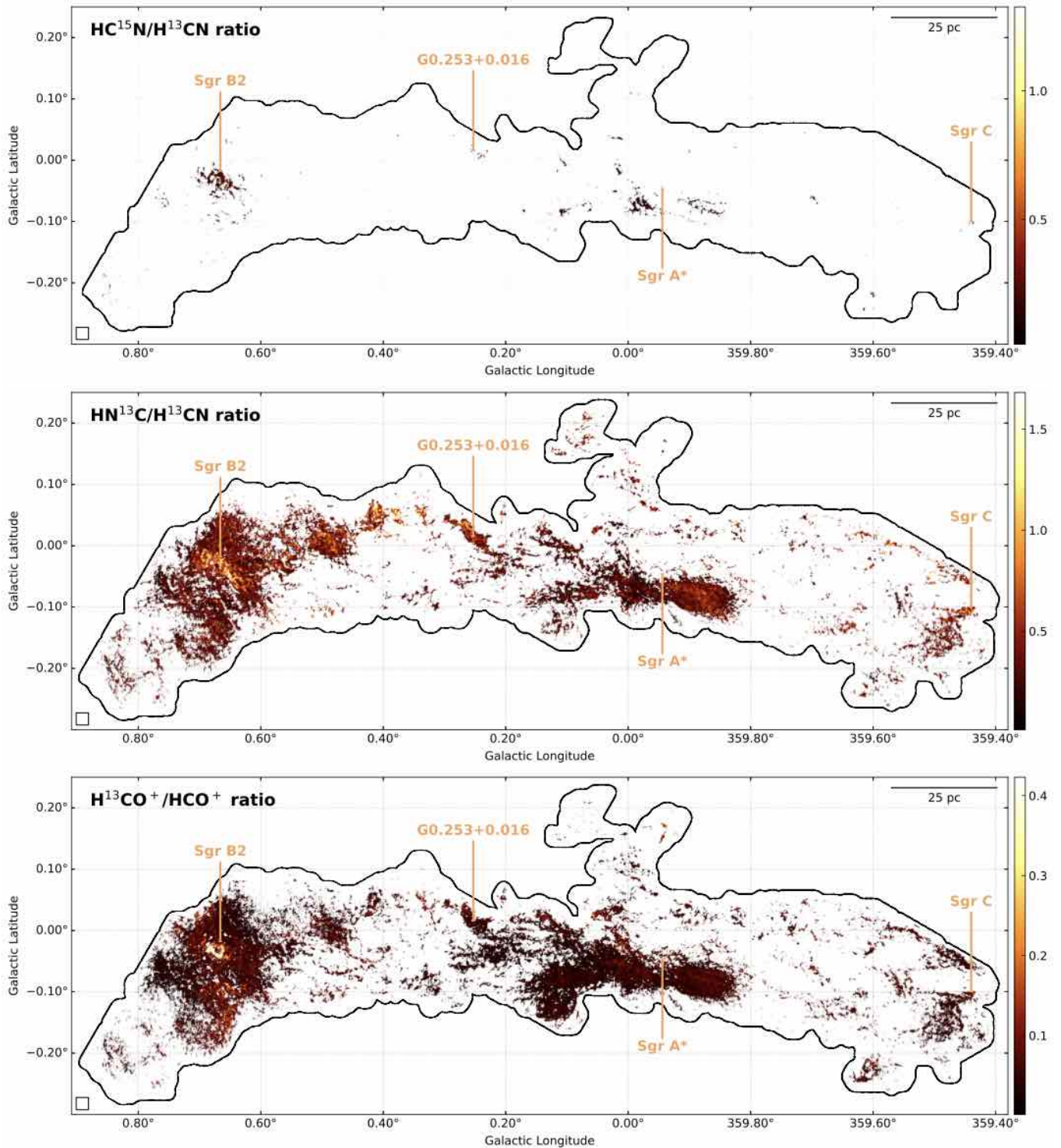


Figure 13. Ratios of integrated brightness temperatures between HC^{15}N 1–0 and H^{13}CN 1–0 (top), HN^{13}C 1–0 and H^{13}CN 1–0 (middle), and H^{13}CO^+ 1–0 and HCO^+ 1–0 (bottom), respectively. The color bars are truncated at the 99.9 percentile of the maximum value.

Team 2026) spectral windows. Note that all papers should be cited for use of any data; the continuum imaging relied on the line papers, and vice-versa.

REFERENCES

- Ao Y., et al., 2013, *A&A*, 550, A135
 Arai H., et al., 2016, *PASJ*, 68, 76
 Astropy Collaboration et al., 2013, *A&A*, 558, A33
 Astropy Collaboration et al., 2022, *ApJ*, 935, 167
 Bachiller R., Pérez Gutiérrez M., 1997, *ApJ*, 487, L93

- Bally J., Stark A. A., Wilson R. W., Henkel C., 1987, *ApJS*, **65**, 13
- Bally J., et al., 2014, *ApJ*, **795**, 28
- Barnes A. T., Longmore S. N., Battersby C., Bally J., Kruijssen J. M. D., Henshaw J. D., Walker D. L., 2017, *MNRAS*, **469**, 2263
- Behrens E., et al., 2022, *ApJ*, **939**, 119
- Borkar A., et al., 2020, in *Multifrequency Behaviour of High Energy Cosmic Sources - XIII*. 3-8 June 2019. Palermo. p. 33 ([arXiv:1909.13753](https://arxiv.org/abs/1909.13753)), doi:10.22323/1.362.0033
- Bouvier M., et al., 2024, *A&A*, **689**, A64
- Busch L. A., Belloche A., Garrod R. T., Müller H. S. P., Menten K. M., 2024, *A&A*, **681**, A104
- CASA Team et al., 2022, *PASP*, **134**, 114501
- Callanan D., et al., 2023, *MNRAS*, **520**, 4760
- Chevance M., Kruijssen J. M. D., Longmore S. N., 2025, *arXiv e-prints*, p. [arXiv:2501.13160](https://arxiv.org/abs/2501.13160)
- Colzi L., Fontani F., Caselli P., Ceccarelli C., Hily-Blant P., Bizzocchi L., 2018, *A&A*, **609**, A129
- Comrie A., et al., 2021, CARTA: Cube Analysis and Rendering Tool for Astronomy, Astrophysics Source Code Library, record ascl:2103.031
- Coutens A., Rawlings J. M. C., Viti S., Williams D. A., 2017, *MNRAS*, **467**, 737
- Eden D. J., et al., 2020, *MNRAS*, **498**, 5936
- Ferrière K., Gillard W., Jean P., 2007, *A&A*, **467**, 611
- Fontani F., Caselli P., Palau A., Bizzocchi L., Ceccarelli C., 2015, *ApJ*, **808**, L46
- GRAVITY Collaboration et al., 2022, *A&A*, **657**, L12
- Ginsburg A., ACES Team 2026, *MNRAS*, **1**, 1
- Ginsburg A., Robitaille T., Beaumont C., 2016a, pvextractor: Position-Velocity Diagram Extractor, Astrophysics Source Code Library, record ascl:1608.010 (ascl:1608.010)
- Ginsburg A., et al., 2016b, *A&A*, **586**, A50
- Ginsburg A., et al., 2019a, radio-astro-tools/spectral-cube: Release v0.4.5, doi:10.5281/zenodo.3558614
- Ginsburg A., et al., 2019b, *AJ*, **157**, 98
- Graninger D. M., Herbst E., Öberg K. I., Vasyunin A. I., 2014, *ApJ*, **787**, 74
- Guan Y., et al., 2021, *ApJ*, **920**, 6
- Hacar A., Bosman A. D., van Dishoeck E. F., 2020, *A&A*, **635**, A4
- Harada N., Saito T., Nishimura Y., Watanabe Y., Sakamoto K., 2024, *ApJ*, **969**, 82
- Harris C. R., et al., 2020, *Nature*, **585**, 357
- Hatchfield H. P., et al., 2024, *ApJ*, **962**, 14
- Henshaw J. D., et al., 2016a, *MNRAS*, **457**, 2675
- Henshaw J. D., Longmore S. N., Kruijssen J. M. D., 2016b, *MNRAS*, **463**, L122
- Henshaw J. D., et al., 2019, *MNRAS*, **485**, 2457
- Henshaw J. D., et al., 2022, *MNRAS*, **509**, 4758
- Henshaw J. D., Barnes A. T., Battersby C., Ginsburg A., Sormani M. C., Walker D. L., 2023, in *Inutsuka S., Aikawa Y., Muto T., Tomida K., Tamura M.*, eds, *Astronomical Society of the Pacific Conference Series Vol. 534, Protostars and Planets VII*. p. 83 ([arXiv:2203.11223](https://arxiv.org/abs/2203.11223)), doi:10.48550/arXiv.2203.11223
- Hirota T., Yamamoto S., Mikami H., Ohishi M., 1998, *ApJ*, **503**, 717
- Hsieh P.-Y., ACES Team 2026, *MNRAS*, **1**, 1
- Huettemeister S., Wilson T. L., Bania T. M., Martín-Pintado J., 1993, *A&A*, **280**, 255
- Hunter J. D., 2007, *Computing in Science and Engineering*, **9**, 90
- Ikeda M., Hirota T., Yamamoto S., 2002, *ApJ*, **575**, 250
- Immer K., Kauffmann J., Pillai T., Ginsburg A., Menten K. M., 2016, *A&A*, **595**, A94
- Inutsuka S., 2021, in *Tsuboi M., Oka T.*, eds, *Astronomical Society of the Pacific Conference Series Vol. 528, New Horizons in Galactic Center Astronomy and Beyond*. p. 271
- Jin M., Lee J.-E., Kim K.-T., 2015, *ApJS*, **219**, 2
- Johnston K. G., Beuther H., Linz H., Schmiedeke A., Ragan S. E., Henning T., 2014, *A&A*, **568**, A56
- Jones P. A., et al., 2008, *MNRAS*, **386**, 117
- Jones P. A., et al., 2012, *MNRAS*, **419**, 2961
- Kauffmann J., Pillai T., Zhang Q., Menten K. M., Goldsmith P. F., Lu X., Guzmán A. E., 2017, *A&A*, **603**, A89
- Koch E., et al., 2025, radio-astro-tools/radio-beam: v0.3.9, doi:10.5281/zenodo.15677957
- Krieger N., et al., 2017, *ApJ*, **850**, 77
- Kruijssen J. M. D., Longmore S. N., Elmegreen B. G., Murray N., Bally J., Testi L., Kennicutt R. C., 2014, *MNRAS*, **440**, 3370
- Kruijssen J. M. D., Dale J. E., Longmore S. N., 2015, *MNRAS*, **447**, 1059
- Kruijssen J. M. D., et al., 2019, *MNRAS*, **484**, 5734
- Krumholz M. R., Kruijssen J. M. D., 2015, *MNRAS*, **453**, 739
- Krumholz M. R., Kruijssen J. M. D., Crocker R. M., 2017, *MNRAS*, **466**, L213
- Li J., An T., Shen Z.-Q., Miyazaki A., 2010, *ApJ*, **720**, L56
- Lis D. C., Serabyn E., Zylka R., Li Y., 2001, *ApJ*, **550**, 761
- Liu H. B., Ho P. T. P., Wright M. C. H., Su Y.-N., Hsieh P.-Y., Sun A.-L., Kim S. S., Minh Y. C., 2013, *ApJ*, **770**, 44
- Longmore S., ACES Team 2026, *MNRAS*, **1**, 1
- Longmore S. N., et al., 2017, *MNRAS*, **470**, 1462
- Lu X., et al., 2017, *ApJ*, **839**, 1
- Lu X., et al., 2019, *ApJS*, **244**, 35
- Lu X., et al., 2021, *ApJ*, **909**, 177
- Lu X., et al., 2024, *ApJ*, **962**, 39
- Mangilli A., et al., 2019, *A&A*, **630**, A74
- Martín-Pintado J., de Vicente P., Fuente A., Planesas P., 1997, *ApJ*, **482**, L45
- Martín-Pintado J., de Vicente P., Rodríguez-Fernández N. J., Fuente A., Planesas P., 2000, *A&A*, **356**, L5
- Martín S., Requena-Torres M. A., Martín-Pintado J., Mauersberger R., 2008, *ApJ*, **678**, 245
- Messineo M., Habing H. J., Sjouwerman L. O., Omont A., Menten K. M., 2002, *A&A*, **393**, 115
- Messineo M., Sjouwerman L. O., Habing H. J., Omont A., 2020, *PASJ*, **72**, 63
- Mills E. A. C., Battersby C., 2017, *ApJ*, **835**, 76
- Mills E. A. C., Morris M. R., 2013, *ApJ*, **772**, 105
- Molinari S., et al., 2011, *ApJ*, **735**, L33
- Nonhebel M., et al., 2024, *A&A*, **691**, A70
- Oka T., Hasegawa T., Sato F., Tsuboi M., Miyazaki A., 1998, *ApJS*, **118**, 455
- Oka T., Nagai M., Kamegai K., Tanaka K., Kuboi N., 2007, *PASJ*, **59**, 15
- Pazukhin A. G., Zinchenko I. I., Trofimova E. A., Henkel C., 2022, *Astronomy Reports*, **66**, 1302
- Pillai T., Kauffmann J., Tan J. C., Goldsmith P. F., Carey S. J., Menten K. M., 2015, *ApJ*, **799**, 74
- Plunkett A., et al., 2023, *PASP*, **135**, 034501
- Price-Whelan A. M., et al., 2018, *AJ*, **156**, 123
- Rathborne J. M., et al., 2014a, *ApJ*, **786**, 140
- Rathborne J. M., et al., 2014b, *ApJ*, **795**, L25
- Requena-Torres M. A., Martín-Pintado J., Rodríguez-Franco A., Martín S., Rodríguez-Fernández N. J., de Vicente P., 2006, *A&A*, **455**, 971
- Requena-Torres M. A., Martín-Pintado J., Martín S., Morris M. R., 2008, *ApJ*, **672**, 352
- Riquelme D., Bronfman L., Mauersberger R., May J., Wilson T. L., 2010a, *A&A*, **523**, A45
- Riquelme D., Bronfman L., Mauersberger R., May J., Wilson T. L., 2010b, *A&A*, **523**, A45
- Robitaille T., Bressert E., 2012, APLpy: Astronomical Plotting Library in Python, Astrophysics Source Code Library (ascl:1208.017)
- Robitaille T., Deil C., Ginsburg A., 2020, reproject: Python-based astronomical image reprojection, Astrophysics Source Code Library, record ascl:2011.023 (ascl:2011.023)
- Sánchez-Monge Á., Schilke P., Ginsburg A., Cesaroni R., Schmiedeke A., 2018, *A&A*, **609**, A101
- Santa-Maria M. G., et al., 2023, *A&A*, **679**, A4
- Sault R. J., Teuben P. J., Wright M. C. H., 1995, in *Shaw R. A., Payne H. E., Hayes J. J. E.*, eds, *Astronomical Society of the Pacific Conference Series Vol. 77, Astronomical Data Analysis Software and Systems IV*. p. 433 ([arXiv:astro-ph/0612759](https://arxiv.org/abs/astro-ph/0612759)), doi:10.48550/arXiv.astro-ph/0612759
- Schilke P., Walmsley C. M., Pineau des Forets G., Flower D. R., 1997, *A&A*, **321**, 293

- Schöier F. L., van der Tak F. F. S., van Dishoeck E. F., Black J. H., 2005, *A&A*, **432**, 369
- Simpson J. P., Colgan S. W. J., Cotera A. S., Kaufman M. J., Stolovy S. R., 2018, *ApJ*, **867**, L13
- Simpson J. P., Colgan S. W. J., Cotera A. S., Kaufman M. J., Stolovy S. R., 2021, *ApJ*, **910**, 59
- Sormani M. C., et al., 2022, *MNRAS*, **512**, 1857
- Stanimirovic S., 2002, in Stanimirovic S., Altschuler D., Goldsmith P., Salter C., eds, *Astronomical Society of the Pacific Conference Series Vol. 278, Single-Dish Radio Astronomy: Techniques and Applications*. pp 375–396 ([arXiv:astro-ph/0205329](https://arxiv.org/abs/astro-ph/0205329), [doi:10.48550/arXiv.astro-ph/0205329](https://doi.org/10.48550/arXiv.astro-ph/0205329))
- Stanimirovic S., Staveley-Smith L., Dickey J. M., Sault R. J., Snowden S. L., 1999, *MNRAS*, **302**, 417
- Tanaka K., Nagai M., Kamegai K., Iino T., Sakai T., 2018, *ApJS*, **236**, 40
- Tress R. G., Sormani M. C., Glover S. C. O., Klessen R. S., Battersby C. D., Clark P. C., Hatchfield H. P., Smith R. J., 2020, *MNRAS*, **499**, 4455
- Walker D., ACES Team 2026, *MNRAS*, **1**, 1
- Wallace J., et al., 2022, *ApJ*, **939**, 58
- Waskom M. L., 2021, *Journal of Open Source Software*, **6**, 3021
- Yang K., et al., 2025, *A&A*, **694**, A86

AUTHOR AFFILIATIONS

- ¹Shanghai Astronomical Observatory, Chinese Academy of Sciences, 80 Nandan Road, Shanghai 200030, P. R. China
- ²State Key Laboratory of Radio Astronomy and Technology, A20 Datun Road, Chaoyang District, Beijing, 100101, P. R. China
- ³UK ALMA Regional Centre Node, Jodrell Bank Centre for Astrophysics, The University of Manchester, Manchester M13 9PL, UK
- ⁴Department of Astronomy, University of Florida, P.O. Box 112055, Gainesville, FL 32611, USA
- ⁵European Southern Observatory (ESO), Karl-Schwarzschild-Straße 2, 85748 Garching, Germany
- ⁶National Astronomical Observatory of Japan, 2-21-1 Osawa, Mitaka, Tokyo 181-8588, Japan
- ⁷Institut de Ciències de l’Espai (ICE), CSIC, Campus UAB, Carrer de Can Magrans s/n, E-08193, Bellaterra, Barcelona, Spain
- ⁸Institut d’Estudis Espacials de Catalunya (IEEC), E-08860, Castelldefels, Barcelona, Spain
- ⁹University of Maryland, Department of Astronomy, College Park, MD 20742-2421, USA
- ¹⁰Max-Planck-Institut für extraterrestrische Physik, Gießenbachstraße 1, 85748 Garching bei München, Germany
- ¹¹Department of Physics and Astronomy, University of Kansas, 1251 Wescoe Hall Drive, Lawrence, KS 66045, USA
- ¹²Astrophysics Research Institute, Liverpool John Moores University, 146 Brownlow Hill, Liverpool L3 5RF, The UK
- ¹³Max Planck Institute for Astronomy, Königstuhl 17, D-69117 Heidelberg, Germany
- ¹⁴Astronomisches Rechen-Institut, Zentrum für Astronomie der Universität Heidelberg, Mönchhofstraße 12-14, D-69120 Heidelberg, Germany
- ¹⁵Cosmic Origins Of Life (COOL) Research DAO, <https://coolresearch.io>
- ¹⁶European Southern Observatory, Alonso de Córdova, 3107, Vitacura, Santiago 763-0355, Chile
- ¹⁷Joint ALMA Observatory, Alonso de Córdova, 3107, Vitacura, Santiago 763-0355, Chile
- ¹⁸School of Astronomy and Space Science, Nanjing University, 163 Xianlin Avenue, Nanjing 210023, P.R.China
- ¹⁹Key Laboratory of Modern Astronomy and Astrophysics (Nanjing University), Ministry of Education, Nanjing 210023, P.R.China
- ²⁰Center for Astrophysics | Harvard & Smithsonian, 60 Garden Street, Cambridge, MA 02138, USA
- ²¹Center for Astrophysics and Space Astronomy, Department of Astrophysical and Planetary Sciences, University of Colorado, Boulder, CO 80389, USA
- ²²Department of Physics, University of Connecticut, 196A Auditorium Road, Unit 3046, Storrs, CT 06269, USA
- ²³Centro de Astrobiología (CAB), CSIC-INTA, Carretera de Ajalvir km 4, 28850 Torrejón de Ardoz, Madrid, Spain
- ²⁴Academia Sinica Institute of Astronomy and Astrophysics, Astronomy-Mathematics Building, AS/NTU No.1, Sec. 4, Roosevelt Rd, Taipei 10617, Taiwan
- ²⁵Space, Earth and Environment Department, Chalmers University of Technology, SE-412 96 Gothenburg, Sweden
- ²⁶Como Lake centre for AstroPhysics (CLAP), DiSAT, Università dell’Insubria, via Valleggio 11, 22100 Como, Italy
- ²⁷Institute of Physics, Laboratory for Galaxy Evolution and Spectral Modelling, EPFL, Observatoire de Sauverny, Chemin Pegasi 51, 1290 Versoix, Switzerland
- ²⁸Observatorio Astronómico de Quito, Observatorio Astronómico Nacional, Escuela Politécnica Nacional, 170403, Quito, Ecuador
- ²⁹INAF Arcetri Astrophysical Observatory, Largo Enrico Fermi 5, Firenze, 50125, Italy
- ³⁰Jodrell Bank Centre for Astrophysics, The University of Manchester, Manchester M13 9PL, UK
- ³¹National Radio Astronomy Observatory, 520 Edgemont Road, Charlottesville, VA 22903, USA
- ³²Universität Heidelberg, Zentrum für Astronomie, Institut für Theoretische Astrophysik, Albert-Ueberle-Str 2, D-69120 Heidelberg, Germany
- ³³Research School of Astronomy and Astrophysics, Australian National University, Canberra, ACT 2611, Australia
- ³⁴Instituto de Astrofísica de Andalucía, CSIC, Glorieta de la Astronomía s/n, 18008 Granada, Spain
- ³⁵Instituto de Astronomía, Universidad Católica del Norte, Av. Angamos 0610, Antofagasta, Chile
- ³⁶Chinese Academy of Sciences South America Center for Astronomy, National Astronomical Observatories, CAS, Beijing 100101, China
- ³⁷Institute for Advanced Study, 1 Einstein Drive, Princeton, NJ 08540, USA
- ³⁸Department of Physics and Astronomy, University College London, Gower Street, London WC1E 6BT, UK
- ³⁹Universität Heidelberg, Interdisziplinäres Zentrum für Wissenschaftliches Rechnen, Im Neuenheimer Feld 225, 69120 Heidelberg, Germany
- ⁴⁰Institute for Research in Fundamental Sciences (IPM), School of Astronomy, Tehran, Iran
- ⁴¹Departamento de Astronomía, Universidad de La Serena, Raúl Bitrán 1305, La Serena, Chile
- ⁴²Instituto de Física Fundamental (CSIC), Calle Serrano 121-123, 28006, Madrid, Spain
- ⁴³Green Bank Observatory, P.O. Box 2, Green Bank, WV 24944, USA
- ⁴⁴Institute of Astronomy, The University of Tokyo, Mitaka, Tokyo 181-0015, Japan
- ⁴⁵Department of Astronomy, University of Massachusetts, Amherst, MA 01003, USA
- ⁴⁶Department of Physics, Aberystwyth University, Ceredigion, Cymru, SY23 3BZ, UK
- ⁴⁷Kavli Institute for Astronomy and Astrophysics, Peking University, Beijing 100871, People’s Republic of China

⁴⁸Department of Astronomy, School of Physics, Peking University,
Beijing, 100871, People's Republic of China

⁴⁹Department of Earth and Planetary Sciences, Institute of Science
Tokyo, Meguro, Tokyo, 152-8551, Japan

APPENDIX A: DATA RELEASE SUMMARY

The data products from the ACES survey follow a uniform naming convention. The filenames for the data products presented in this paper can be constructed using the templates described below, in conjunction with the information provided in Appendix A of [Walker & ACES Team \(2026\)](#).

The following subsections are divided according to different product types which occur at the Member ObsUnitSet (MOUS) and Group ObsUnitSet (GOUS) levels³.

A1 Member-level products (12m and 7m)

We release the data cubes for all SPWs for the 45 ACES regions. These are member-level products, and correspond to the cubes for the 12m and 7m arrays for each field prior to combination.

We release the cubes for the separate arrays as they are different to those initially delivered by ALMA due to the changes that were made during reprocessing. We do not re-release any of the stand-alone TP products, as we used the same cubes as those available in the ALMA Science Archive (ASA).

In this and subsequent subsections, we describe how to construct the filenames of the released data products by providing filename templates that include placeholder variables. These placeholders can be changed as needed to build the filename of the relevant product.

Following the requirements of the ASA, the filename template is:

```
member.uid__A001_{mous-id}.lp_2021.1.00172.L.slongmore.{field_coords}.{array}.{frqrange}.cube.pbcor.fits
```

The placeholder template components should be replaced as follows:

- **{mous-id}**: The 12m or 7m MOUS ID for a given field, as listed in Table A1 in [Walker & ACES Team \(2026\)](#).
- **{field_coords}**: The central coordinates of the field, as listed in Table A1 in [Walker & ACES Team \(2026\)](#) (e.g., G000.073+0.184).
- **{array}**: The ALMA array, either 12m or 7m.
- **{frqrange}**: The frequency range, which depends on the SPW:
 - SPW 25: 86.0–86.4GHz
 - SPW 27: 86.7–87.1GHz

For example, to find the 12m-only cube for the 12-m SPW 25 for field ao (this field contains the well-known molecular cloud G0.253+0.016, aka the Brick), the resulting filename would be:

```
member.uid__A001_X15a0_X190.lp_2021.1.00172.L.slongmore.G000.300+0.063.12m.86.0-86.4GHz.cube.pbcor.fits
```

A2 Group-level products (Combined cubes per region)

We also release array-combined products per SPW per region. As these products combine data from multiple MOUSs, they are deemed to be group-level products. The filenames of these products can be constructed as follows:

```
group.uid__A001_X1590_X30a9.lp_2021.1.00172.L.slongmore.{field_coords}.{arrays}.{frqrange}.cube.pbcor.fits
```

Where the template components are:

- **{field_coords}** and **{frqrange}**: follow the same definition as for the member-level products.
- **{arrays}**: 12m7mTP

For example, the corresponding 12-m SPW 25 cube including 12m, 7m, and TP data for field ao would be:

```
group.uid__A001_X1590_X30a9.lp_2021.1.00172.L.slongmore.G000.300+0.063.12m7mTP.86.0-86.4GHz.cube.pbcor.fits
```

A summary of the combined cubes for the two intermediate-width SPWs, including the original beam shapes, pixel sizes, and imaging rms of the individual fields, is reported in Tables A1 and A2.

A3 Group-level products (Full CMZ mosaics)

Finally, we release the full, contiguous mosaics covering the entire ACES footprint. Again, since these result from the combination of many MOUSs, the full mosaics are at the group level.

In contrast to cubes for the individual fields, we do not release full mosaics for all SPWs, but rather for the 6 specific lines given in [Table 1](#). The SPWs are sufficiently broad that they contain significant spectral ranges with no line emission. We therefore opted to not produce full mosaics containing these blank channels in the interest of reducing the file sizes. In addition to the data cubes for each line, we also release a suite of advanced products, including moment maps, noise maps, etc. (see below).

The filename template for the full mosaic cubes and associated products is:

```
group.uid__A001_X1590_X30a9.lp_2021.1.00172.L.slongmore.cmz_mosaic.{arrays}.{molecule}.{suffix}
```

Where the template components are:

³ For a description of ALMA project structures and naming conventions, please refer to Section 2 of the Cycle 9 QA2 guide: <https://almascience.eso.org/documents-and-tools/cycle9/alma-qa2-data-products-for-cycle-9>

- `{arrays}`: 12m7mTP
- `{molecule}`: H13CN, H13COplus, HC15N, HN13C, SiO21, or SO21.
- `{suffix}` defines the specific data product. Products released with this paper are:
 - `cube.pbcor.fits`: primary beam corrected image cube.
 - `cube.downsampled_spatially.pbcor.fits`: as previous, spatially smoothed to a 5 arcsec beam and then spatially rebinned by a factor of 9×9 .
 - `integrated_intensity.fits`: masked integrated intensity map of the full-resolution cube.
 - `mad_std.fits`: noise map of the full-resolution cube.
 - `peak_intensity.fits`: peak intensity map of the full-resolution cube.
 - `velocity_at_peak_intensity.fits`: velocity map from the masked full-resolution cube; velocity estimated using the peak intensity of the spectrum for each pixel.
 - `PV_l_max.fits`: ℓ - v position-velocity map from the full-resolution cube; maximum intensity taken along Galactic latitude (b).
 - `PV_l_mean.fits`: ℓ - v position-velocity map from the masked full-resolution cube; mean intensity taken along Galactic latitude (b).
 - `PV_b_max.fits`: b - v position-velocity map from the full-resolution cube; maximum intensity taken along Galactic longitude (ℓ).
 - `PV_b_mean.fits`: b - v position-velocity map from the full-resolution cube; mean intensity taken along Galactic longitude (ℓ).

As an example, the peak ℓ - v map for the full ACES mosaic of the combined SiO (2–1) data would be constructed as:
`group.uid__A001_X1590_X30a9.lp_2021.1.00172.L.slongmore.cmz_mosaic.12m7mTP.SiO21.PV_l_max.fits`

APPENDIX B: ARRAY COMBINATION USING MIRIAD

The 12-m array, the 7-m array, and the Total Power (TP) array of ALMA each are each only sensitive to a certain range of angular scales. To recover the multi-scale gas structures in the CMZ from 0.1 pc ($2''$) to over 200 pc, it is necessary to combine data from the different arrays and produce images that are sensitive to both small and large angular scales. Such a procedure, usually referred to as ‘array combination’, can be implemented in different approaches, e.g., concatenating visibility data and CLEANing them to obtain an image (‘joint imaging’), or linearly combining the images from different arrays (‘feathering’). The ACES data releases took the latter approach and produced the combined images (Paper II; Paper III). A detailed discussion on the array combination can be found in Plunkett et al. (2023).

One of the reasons why we chose feathering over joint imaging is that joint imaging in CASA is computationally more expensive and slower, and often diverges. Meanwhile, array combination can be implemented in other packages, e.g., Miriad (Stanimirovic et al. 1999; Stanimirovic 2002).

Here, we present an experiment of joint imaging using Miriad, on the SiO (2–1) line in one of the regions that cover the G0.253–0.016 cloud. The joint imaging is implemented with a modified ALMICA procedure⁴, which is forked from the original version⁵ by Hauyu Baobab Liu (Liu et al. 2013). The workflow consists of the following major steps:

- (i) Deconvolve the TP image to obtain a CLEAN model for each of the 7-m pointings, using the CLEAN and DEMOS tasks.
- (ii) Generate artificial visibility data from the TP CLEAN model, using the UVRANDOM and UVMODEL tasks. Adjust the weight of the TP visibility data through manipulating the system temperature, using the UVPUTHD task.
- (iii) Image the TP and 7-m visibilities together to obtain a CLEAN model for the whole mosaic, using the INVERT and MOSSDI tasks.
- (iv) Decompose the TP+7-m CLEAN model for the mosaic to that for each of the 12-m pointings, using the DEMOS task. Generate artificial visibility data from the CLEAN model for individual 12-m pointings, using the UVRANDOM and UVMODEL tasks. Adjust the weight of the TP+7-m visibility data through manipulating the system temperature, using the UVPUTHD task.
- (v) Finally, image the TP+7-m and 12-m visibilities together to obtain the combined image, using the INVERT, MOSSDI, and RESTOR tasks.
- (vi) There is an optional step to further merge the TP image with the combined image, using the IMMERGE task. This linear combination in the image domain is similar to the feathering method in CASA.

For detailed steps, readers are referred to Appendix A of Liu et al. (2013) and the ALMICA github repository.

We follow the above workflow, and set a system temperature of 500 K for both the TP and the 7-m visibilities. In step 2, we generate 500 data points for the artificial TP visibility data, which are uniformly distributed in the uv plain within a maximum baseline length of 12 m. Similarly, in step 4, we generate 3000 data points for the artificial TP+7-m visibility data uniformly distributed in the uv plain within a maximum baseline length of 45 m. The resulting combined images with and without the optional IMMERGE step are shown in Figures B1–B3. We also show the combined image from the feathering approach and the TP image for comparison. The beam sizes and image RMS of the three approaches are summarised in Table B1.

It can be seen that the combined images made with ALMICA and CASA-feather are broadly consistent in terms of the morphology, although some nuances can still be found. The ALMICA image clearly shows negative bowls around bright emission peaks, which are signatures of missing flux (Plunkett et al. 2023). With the additional IMMERGE step, ALMICA imaging performs better in terms of mitigating the negative bowls. The CASA-feather image performs the best in recovering diffuse emission, where the negative bowls are mostly gone.

In Figure B4 we compare spectra from different array combination approaches. Spectra from the TP image and from the 12-m array only image (made with the CASA *tclean* task) are also plotted for comparison. The ALMICA image clearly recovers more flux than the 12-m array

⁴ <https://github.com/xinglunju/almica>

⁵ <https://github.com/baobabyoo/almica>

Table A1. Global statistics for the 12-m SPW 25 cubes, after feathering data from the 12-m, 7-m, and TP arrays altogether, for all ACES fields. The noise is estimated from channels in the lowest quartile of the mean spectrum (assumed emission-free) using the scaled median absolute deviation (MAD; where $\sigma_{\text{MAD}} = 1.4826\text{MAD}$).

Field	V_{off} (km s^{-1})	B_{maj} ($''$)	B_{min} ($''$)	BPA ($^{\circ}$)	Image size (pix)	No. channels	Pixel size ($''$)	S_{peak} (mJy beam^{-1})	σ_{MAD} (mJy beam^{-1})	S_{peak} (K)	σ_{MAD} (K)
a	40	1.69	1.20	-77	(2094, 2499)	1912	0.20	454.3	5.2	36.9	0.4
aa	0	2.04	1.74	-75	(1623, 1481)	1917	0.26	1527.0	4.7	70.9	0.2
ab	0	1.99	1.70	88	(1496, 1261)	1915	0.28	729.3	4.5	35.5	0.2
ac	0	1.78	1.20	-78	(1686, 1626)	1914	0.19	987.6	5.2	76.2	0.4
ad	0	2.02	1.19	-75	(1184, 2564)	1920	0.20	668.7	5.7	45.8	0.4
ae	0	2.26	1.84	83	(1343, 1365)	1914	0.30	849.2	4.9	33.6	0.2
af	0	2.79	1.71	89	(1446, 1176)	1915	0.31	1009.9	5.0	34.9	0.2
ag	0	1.91	1.46	-79	(1731, 1721)	1912	0.24	6629.9	5.0	391.6	0.3
ah	30	1.87	1.20	-72	(2004, 1942)	1912	0.20	600.8	4.4	44.1	0.3
ai	0	2.55	1.77	78	(1378, 1622)	1914	0.29	1217.4	4.6	44.4	0.2
aj	-30	2.45	1.79	85	(1439, 1288)	1914	0.31	20814.4	4.4	781.8	0.2
ak	30	2.48	2.11	82	(764, 1009)	1916	0.32	448.6	4.8	14.1	0.2
al	0	2.77	2.04	86	(2190, 1447)	1920	0.28	679.6	5.8	19.8	0.2
am	30	3.14	1.98	-85	(2612, 1140)	1920	0.30	622.9	6.3	16.5	0.2
an	30	2.55	1.73	83	(1335, 1359)	1914	0.30	4246.9	5.1	158.6	0.2
ao	0	2.52	1.62	-86	(2512, 923)	1914	0.28	2742.1	6.0	110.6	0.2
ap	0	2.30	1.87	79	(1344, 1371)	1914	0.30	814.0	4.4	31.2	0.2
aq	0	1.72	1.36	-85	(1828, 1815)	1915	0.22	1018.6	5.1	71.7	0.4
ar	40	2.38	1.78	84	(1389, 1423)	1915	0.29	584.9	5.4	22.7	0.2
as	0	1.98	1.33	-76	(2009, 2053)	1915	0.20	582.0	5.3	36.4	0.3
b	40	1.78	1.41	86	(1915, 1958)	1915	0.21	2213.5	4.2	145.3	0.3
c	0	2.73	1.79	87	(1435, 1461)	1915	0.28	647.8	5.8	21.8	0.2
d	30	1.94	1.55	-63	(2061, 1585)	1917	0.23	1619.4	5.5	88.7	0.3
e	-30	2.84	1.76	-90	(1442, 1472)	1915	0.28	1147.9	5.5	37.8	0.2
f	0	2.89	1.73	90	(1782, 1468)	1920	0.28	1016.9	5.6	33.5	0.2
g	30	2.24	1.67	84	(1606, 1647)	1915	0.25	1025.7	5.0	45.2	0.2
h	0	1.73	1.27	-84	(1994, 2114)	1912	0.21	620.9	4.8	46.6	0.4
i	30	1.75	1.53	-67	(1682, 1641)	1912	0.25	736.3	4.4	45.3	0.3
j	30	2.83	1.68	-88	(1480, 1510)	1915	0.27	970.3	5.9	33.6	0.2
k	30	1.90	1.11	-80	(2227, 2207)	1912	0.18	2283.9	5.5	178.4	0.4
l	0	1.85	1.65	-80	(2419, 1525)	1915	0.26	805.5	4.8	43.5	0.3
m	30	2.57	2.12	82	(1373, 1377)	1917	0.29	3644.8	4.5	110.2	0.1
n	30	1.85	1.14	-82	(1406, 1844)	1914	0.19	580.8	5.6	45.4	0.4
o	0	2.73	1.89	-89	(1310, 1252)	1915	0.32	1503.	5.5	48.0	0.2
p	0	1.70	1.23	86	(2078, 2057)	1915	0.20	687.8	4.9	54.2	0.4
q	0	2.43	1.86	88	(1345, 1367)	1915	0.30	464.4	4.3	16.9	0.2
r	30	3.16	1.90	-83	(1556, 1419)	1917	0.29	820.8	5.1	22.5	0.1
s	0	2.78	1.99	87	(1339, 1369)	1917	0.30	1450.5	5.2	43.2	0.2
t	0	2.31	1.95	74	(1297, 1293)	1914	0.31	792.8	5.1	29.0	0.2
u	30	2.06	1.21	-75	(1394, 2088)	1914	0.19	729.5	6.0	48.2	0.4
v	30	1.94	1.23	-81	(1410, 1916)	1914	0.19	126.7	5.4	8.7	0.4
w	30	2.47	1.74	-82	(1508, 1424)	1915	0.28	680.6	4.6	26.1	0.2
x	0	2.67	1.88	-88	(1321, 790)	1916	0.30	514.1	5.2	16.9	0.2
y	0	2.34	1.78	-86	(1464, 1138)	1917	0.27	378.3	5.5	15.0	0.2
z	40	2.61	1.63	82	(1382, 1377)	1915	0.29	617.2	5.3	23.9	0.2

only one. However, it does not recover all of the expected flux based on the TP image. The ALMICA image with the additional IMMERGE step and the CASA-feather image perform better when it comes to recovering the flux of the TP image.

To summarize, the experiment suggests that the ALMICA approach with the additional IMMERGE step performs equally well at mitigating negative bowls and recovering the missing flux as compared to the CASA-feather approach, but at a computing speed of about 10 times faster. The drawbacks of ALMICA, however, include its reliance on the Miriad package, which has a smaller user community than CASA, and its current lack of parallelisation.

Table A2. Global statistics for the 12-m SPW 27 cubes, after feathering data from the 12-m, 7-m, and TP arrays altogether, for all ACES fields. The noise is estimated from channels in the lowest quartile of the mean spectrum (assumed emission-free) using the scaled median absolute deviation (MAD; where $\sigma_{\text{MAD}} = 1.4826\text{MAD}$).

Field	V_{off} (km s^{-1})	B_{maj} ($''$)	B_{min} ($''$)	BPA ($^{\circ}$)	Image size (pix)	No. channels	Pixel size ($''$)	S_{peak} (mJy beam^{-1})	σ_{MAD} (mJy beam^{-1})	S_{peak} (K)	σ_{MAD} (K)
a	40	1.74	1.19	-77	(2091, 2498)	1912	0.20	89.1	4.7	7.0	0.4
aa	0	2.08	1.73	-75	(1620, 1479)	1917	0.26	160.4	4.6	7.2	0.2
ab	0	1.97	1.69	89	(1494, 1259)	1914	0.28	123.2	4.4	6.0	0.2
ac	0	1.78	1.21	-79	(1683, 1624)	1914	0.19	122.0	5.1	9.2	0.4
ad	0	2.01	1.18	-76	(1182, 2562)	1920	0.20	106.2	5.6	7.3	0.4
ae	0	2.28	1.84	82	(1341, 1364)	1914	0.30	126.0	4.7	4.9	0.2
af	0	2.84	1.68	-90	(1443, 1174)	1915	0.31	245.9	5.0	8.4	0.2
ag	0	1.90	1.45	-79	(1729, 1719)	1912	0.24	138.8	4.9	8.2	0.3
ah	30	1.86	1.20	-72	(2001, 1939)	1914	0.20	102.8	4.3	7.5	0.3
ai	0	2.57	1.76	80	(1376, 1620)	1914	0.29	161.2	4.6	5.8	0.2
aj	-30	2.42	1.77	84	(1438, 1286)	1914	0.31	172.1	4.3	6.5	0.2
ak	30	2.47	2.08	83	(762, 1007)	1916	0.32	173.6	4.7	5.5	0.1
al	0	2.75	2.03	86	(2189, 1446)	1920	0.28	187.6	5.6	5.4	0.2
am	30	3.22	1.97	-84	(2610, 1138)	1920	0.30	238.7	6.3	6.1	0.2
an	30	2.52	1.72	83	(1333, 1357)	1914	0.30	1114.7	5.0	41.7	0.2
ao	0	2.52	1.62	-87	(2509, 921)	1914	0.28	177.2	5.9	7.0	0.2
ap	0	2.27	1.86	79	(1342, 1369)	1914	0.30	143.0	4.3	5.5	0.2
aq	0	1.72	1.34	-84	(1826, 1813)	1915	0.22	125.7	5.0	8.8	0.4
ar	40	2.35	1.77	84	(1386, 1423)	1914	0.29	157.5	5.3	6.1	0.2
as	0	2.00	1.31	-75	(2005, 2051)	1915	0.20	156.9	5.2	9.7	0.3
b	40	1.76	1.40	85	(1913, 1956)	1915	0.21	837.0	4.1	55.1	0.3
c	0	2.74	1.78	87	(1433, 1459)	1915	0.28	155.7	5.6	5.2	0.2
d	30	1.96	1.53	-65	(2058, 1582)	1917	0.23	105.6	5.4	5.7	0.3
e	-30	2.94	1.80	87	(1441, 1471)	1915	0.28	175.7	5.5	5.4	0.2
f	0	2.85	1.72	90	(1780, 1466)	1920	0.28	222.3	5.4	7.4	0.2
g	30	2.27	2.26	85	(1603, 1644)	1915	0.25	193.6	4.8	6.1	0.2
h	0	1.70	1.25	-84	(1991, 2112)	1912	0.21	174.3	4.8	13.3	0.4
i	30	1.73	1.52	-70	(1678, 1639)	1912	0.25	141.8	4.4	8.7	0.3
j	30	2.83	1.65	-87	(1477, 1508)	1915	0.27	209.7	5.9	7.3	0.2
k	30	1.89	1.09	-79	(2223, 2202)	1912	0.18	113.5	5.5	8.9	0.4
l	0	1.84	1.63	-79	(2417, 1522)	1915	0.26	248.0	4.7	13.4	0.3
m	30	2.55	2.10	81	(1372, 1376)	1917	0.29	2547.4	4.4	77.1	0.1
n	30	1.80	1.12	-79	(1403, 1842)	1914	0.19	99.8	5.4	8.0	0.4
o	0	2.82	1.91	86	(1308, 1251)	1915	0.32	333.3	5.5	10.0	0.2
p	0	1.82	1.35	84	(1887, 1868)	1915	0.22	130.3	4.4	8.6	0.3
q	0	2.41	1.85	88	(1343, 1365)	1914	0.30	199.3	4.2	7.2	0.2
r	30	3.25	1.91	-86	(1555, 1417)	1917	0.29	204.3	5.0	5.3	0.1
s	0	2.75	1.99	86	(1337, 1367)	1917	0.30	229.0	5.0	6.8	0.1
t	0	2.31	1.94	73	(1295, 1292)	1914	0.31	149.8	4.9	5.4	0.2
u	30	2.04	1.21	-75	(1392, 2085)	1914	0.19	116.8	5.9	7.7	0.4
v	30	1.92	1.22	-81	(1407, 1913)	1914	0.19	115.1	5.3	8.0	0.4
w	30	2.45	1.73	-82	(1506, 1423)	1914	0.28	123.8	4.5	4.7	0.2
x	0	2.64	1.86	-88	(1318, 790)	1916	0.30	154.5	5.2	5.1	0.2
y	0	2.28	1.66	-88	(1462, 1136)	1915	0.27	128.4	5.6	5.5	0.2
z	40	2.59	1.63	82	(1380, 1375)	1914	0.29	138.9	5.1	5.3	0.2

Table B1. Imaging parameters and properties of the combined SiO (2-1) images from ALMICA and CASA-feathering.

Combination method	Beam size & PA ($'' \times ''$, $^{\circ}$)	Image RMS (mJy beam^{-1} per 0.85 km s^{-1})
Miriad-ALMICA	2.58×1.91 , -88.24	4.0
Miriad-ALMICA-immerge	2.58×1.91 , -88.24	4.0
CASA-feathering	2.52×1.62 , -86.95	4.2

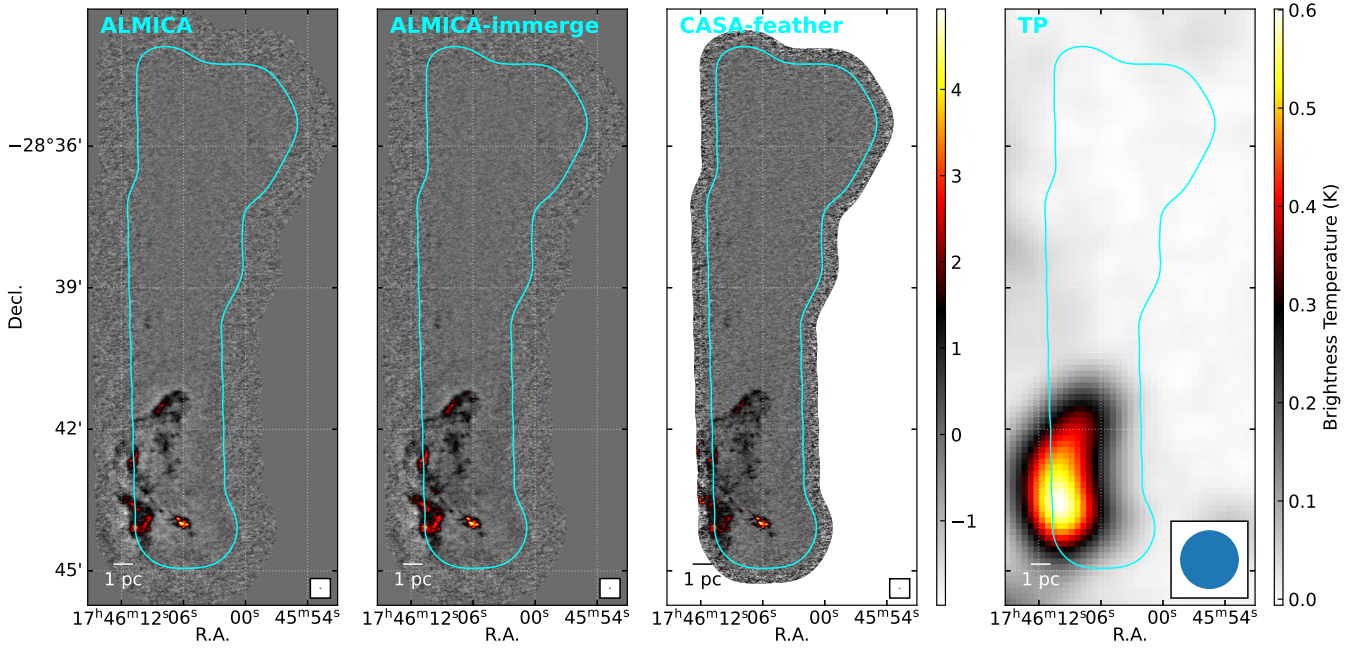


Figure B1. SiO images of a velocity channel at $\sim 30 \text{ km s}^{-1}$ from different array combination approaches. The velocity is close to be around the systemic velocity of the cloud and show complex structures in emission. The three array-combined images are adjusted to the same color scale. The TP image with a different color scale is also shown for reference. Primary-beam response at the 0.5 level of the 12-m array mosaic is shown as a cyan contour in all panels.

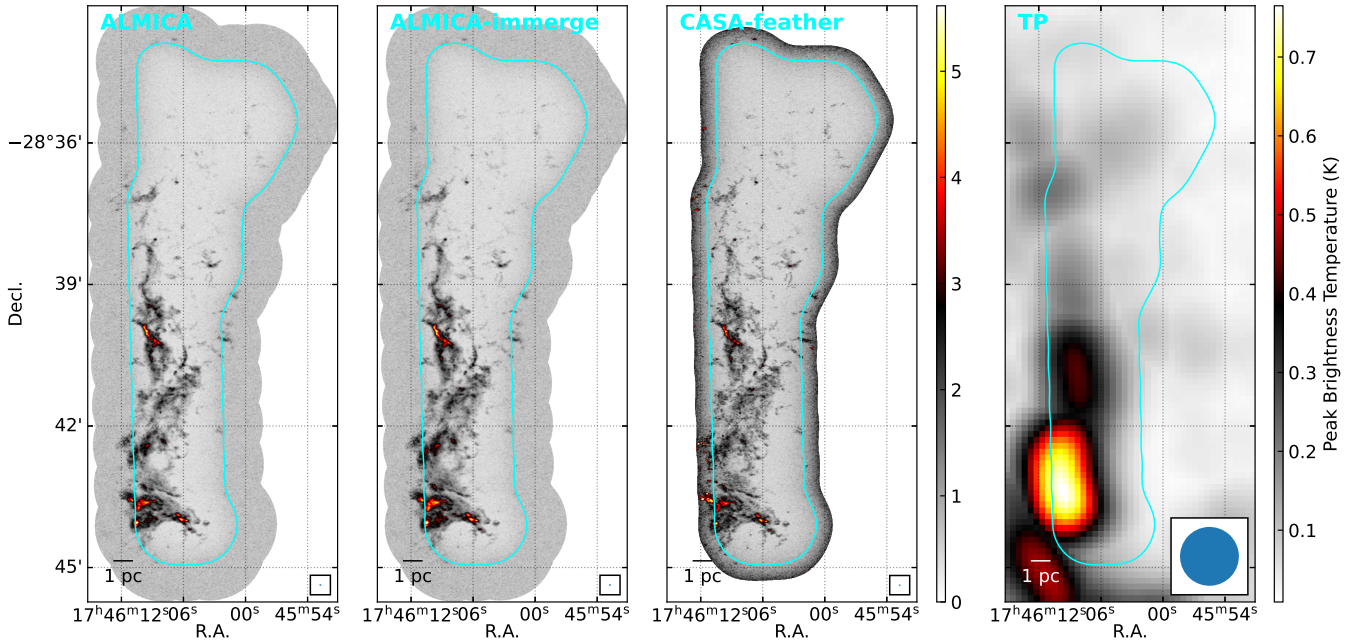


Figure B2. Peak brightness temperatures of the SiO (2–1) line, from different array combination approaches with the same color scale, and from the TP array with a different color scale for reference.

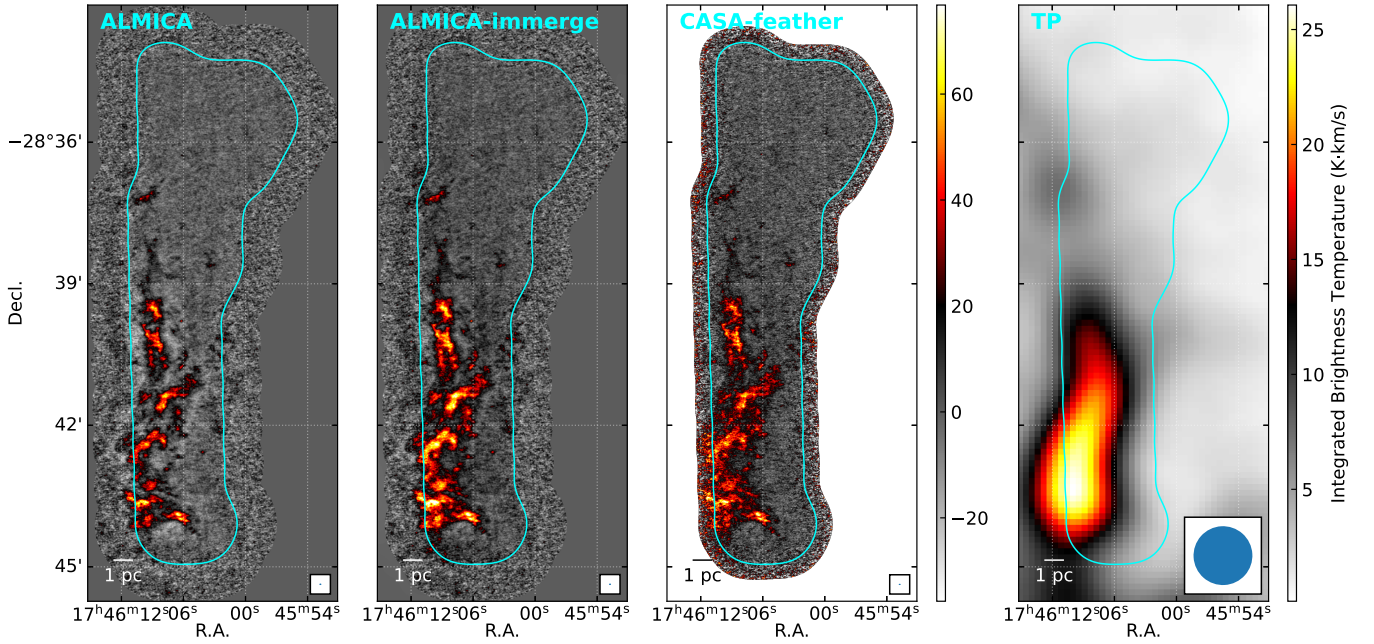


Figure B3. Integrated brightness temperatures of the SiO (2–1) line, from different array combination approaches with the same color scale, and from the TP array with a different color scale for reference. The images are integrated between $V_{\text{LSR}} = -100$ and 200 km s^{-1} .

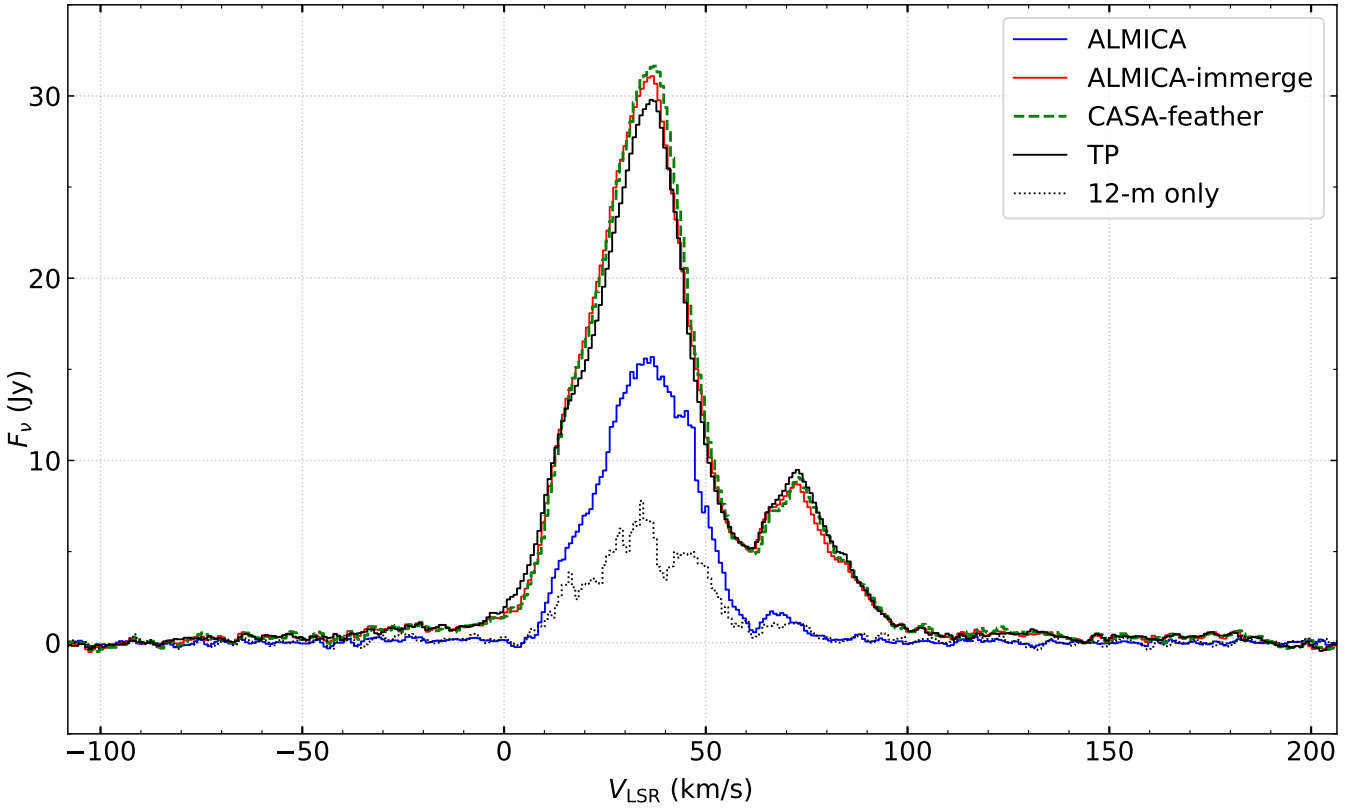


Figure B4. SiO (2–1) spectra with flux densities in the y-axis within a circle of a radius of $74''.8$, which is the beam size of the TP image, centered at the peak of the integrated brightness temperature map (RA, Dec. = $17:46:06.57$, $-28:43:52.12$ in the ICRS frame). Spectra from the three different array combination approaches, as well as those from the TP image and the 12-m array only image are also plotted for references.

This paper has been typeset from a \TeX/L\AA\TeX file prepared by the author.